ADDITIVE MANUFACTURING OF A FORWARD METERING STRUCTURE FOR SPACE IMAGING APPLICATIONS

Marvin Calderon **Arden Gao** **Ethan Sanna** **Jake Snyder**

ABSTRACT

Additive manufacturing (AM) is increasingly being used in aerospace applications because it enables complex, lightweight geometries that are difficult or impractical to produce using traditional subtractive manufacturing. This project, sponsored by L3Harris, focused on the design, analysis, and prototype development of an additively manufactured forward metering structure (FMS) for a space-based optical imaging system. Additive manufacturing is advantageous as it allows for "economic efficiency, unparalleled design freedom, high customizability… and the ability to process a wide range of materials including metals" [1]. The FMS serves as the structural element that supports and positions the secondary mirror (SM) above the primary mirror (PM), making stiffness, alignment stability, thermal performance, vibration resistance, mass efficiency, and optical obscuration critical design considerations. Throughout the project, the team has developed and evaluated multiple design iterations using hand calculations, CAD modeling, finite element analysis (FEM), material testing, vendor and sponsor manufacturability feedback, prototype fabrication, and physical testing. The team worked closely with the team at L3Harris, Professor Muir, and the University of Rochester's Mechanical Engineering department to simulate several iterations, test and validate materials, manufacture and construct a prototype, and successfully provide L3Harris with a final design. This report documents the design process, analysis methods, prototype development, testing, and final recommendations provided to L3Harris.

PROBLEM DEFINITION

The purpose of this project is to design and fabricate a 3D metal-printed forward metering structure (FMS) to connect and align the primary and secondary mirrors for a space-based optical satellite system. L3Harris has requested a design optimized for additive manufacturing to reduce build time while maintaining critical structural performance. This process allows the FMS to be fabricated as a monolithic part in a single build cycle, rather than as a complex multi-component assembly. This approach also encourages the team to incorporate advanced geometries that would not be practical with common manufacturing techniques but could be easily achieved with 3D printing. It's important to recognize that modest performance trade-offs will take place; however, the purpose of this project is to demonstrate a fast, repeatable, and cost-effective solution for the future of space-based technologies. The team's final deliverable will consist of a tested prototype and correlated model that meets industry requirements.

REQUIREMENTS, SPECIFICATIONS, DELIVERABLES

I. Requirements

1. **[UR-FMS-004]** The FMS shall define a clear, traceable primary load path from the Secondary Mirror interface to the AMS interface. All major load-bearing members shall be identified in the structural model and correlated to physical geometry.
2. **[UR-FMS-005]** The FMS material shall be Invar (or an Invar-class alloy) to minimize coefficient of thermal expansion (CTE) driven misalignment. (See Overview document for values)
3. **[UR-FMS-010]** The FMS should incorporate redundancy or fault-tolerant load paths where required by mission assurance analysis, such that no single credible structural failure results in loss of SM containment or gross misalignment.
4. **[UR-FMS-011]** The FMS shall be produced using additive manufacturing. The design shall incorporate controlled additive manufacturing process parameters sufficient to support topology and lattice optimization, model-to-test correlation, thermal stability characterization, and repeatable manufacturability.
5. **[UR-FMS-012]** The FMS shall be designed to print vertically with the AMS interface side on the build plate. Support structures are permitted but undesirable; any required supports shall be limited to non–optical-critical surfaces and shall be fully removable without damage to functional interfaces.

6. **[UR-FMS-013]** The FMS shall be designed to ensure there are no trapped cavities or unvented volumes that could retain contamination, inhibit precision cleaning, or create pressure differentials.
7. **[UR-FMS-014]** The FMS shall include handling features or zones to support safe lifting, fixturing, and inspection without imparting loads through optical interfaces. (These features will likely need to be near the AMS interface, below the primary mirror)
8. **[UR-FMS-015]** For any hollow-shell or lattice designs, the FMS shall include contamination control features (e.g., vent mesh) to prevent debris migration to optical surfaces and shall permit inspection and verification of these features.
9. **[UR-FMS-016]** The FMS shall define and maintain a controlled datum scheme and provide metrology features enabling repeatable measurement of SM position relative to the AMS.
10. **[UR-FMS-017]** The FMS shall define interfaces for the following hosted hardware.
11. **[UR-FMS-018]** The FMS should recommend routing and mounting locations for thermal hardware associated with the Secondary Mirror (SM) and shade assembly (Heater tapes, thermistors, cabling) while maintaining defined optical and baffle keep-out zones.
12. **[UR-FMS-019]** All FMS surfaces visible to the optical cavity shall meet stray-light requirements, including low-reflectance finishes, non-flaking coatings, and avoidance of specular glint paths to the focal plane.

II. Specifications

1. **[UR-FMS-001]** The Forward Metering Structure (FMS) and Secondary Mirror (SM) shall have positive margins of safety against yield and ultimate failure when subjected to quasi-static launch loads of a 30 g spherical sweep, swept at 15-degree increments, while supporting all hosted hardware. Launch loads shall be combined with a 5°C to 35°C temperature range. Structural performance shall be demonstrated across these environments and shall include all credible load paths and boundary conditions at the AMS interface.
2. **[UR-FMS-002]** The FMS and SM shall meet the following minimum structural factors of safety unless superseded by higher-level program requirements:
    a. Yield ≥ 2.0
    b. Ultimate ≥ 2.5
        i. Ultimate Glass ≥ 5
    c. Buckling ≥ 4.0
    d. If a micro-yield criterion is used, the criterion shall be defined (e.g., strain-based), and the micro-yield factor of safety shall be ≥ 1.0 for all applicable load cases.
3. **[UR-FMS-003]** The FMS shall provide a stable mounting platform for the Secondary Mirror (SM) (assumed via blade flexures). Under a 1°C isothermal temperature change, the average motion of the SM interface shall be limited to:
    a. 0.2 µm (7.87 micro inches) translation (RSS of X and Y), and
    b. 0.9 µrad rotation (RSS of Rx and Ry)
4. **[UR-FMS-006]** Mass < 25 lbm, inclusive of structural material and permanently attached features, and exclusive of hosted hardware. The following mass growth allowances shall be applied for design gate reviews:
    a. Concept design: 20%
    b. Preliminary design: 15%
    c. Final design: 10%
    d. Post–Final Design: 5%
    e. As-built measured hardware: 0.10%
5. **[UR-FMS-007]** First structural mode of the FMS shall be 60 Hz or greater (greater than 100 Hz desired) when constrained at the AMS interface and supporting all hosted hardware, including representative joint stiffness and preload assumptions. (See MICD for detailed weights)
    a. The AMS interface is defined as being 35” from the back side of the Secondary Mirror (SM)
    b. Explicitly document assumed joint stiffness, boundary conditions, and interface preload values at the AMS and SM interfaces. Sensitivity of the first mode frequency to joint stiffness assumptions shall be assessed.
6. **[UR-FMS-020]** The FMS shall have a maximum of 22% total obscuration area of the entrance pupil of the Primary Mirror (PM) (assuming a 0.8m diameter clear aperture). (Compliance may be demonstrated using geometric ray-blocking diagrams and projected area calculations; optical modeling is not required)

III. Deliverables

1. **[CDRL-UR-001]** CAD file prototypes using NX (step file format) and 2D drawings
2. **[CDRL-UR-002]** Finite Element Model (FEM) in Nastran
3. **[CDRL-UR-003]** Final design report
4. **[CDRL-UR-004]** Host design review meetings and provide supporting slides and drops of the CAD and FEM
5. **[CDRL-UR-005]** Concept Design Review (CDR)
6. **[CDRL-UR-006]** Preliminary Design Review (PDR)
7. **[CDRL-UR-007]** Final Design Review (FDR)
8. **[CDRL-UR-008]** 3D printed prototype
9. **[CDRL-UR-009]** Reports on any model validation (ex. Modal test, stiffness/deflection test, etc.) - could be included in design review slides and final report

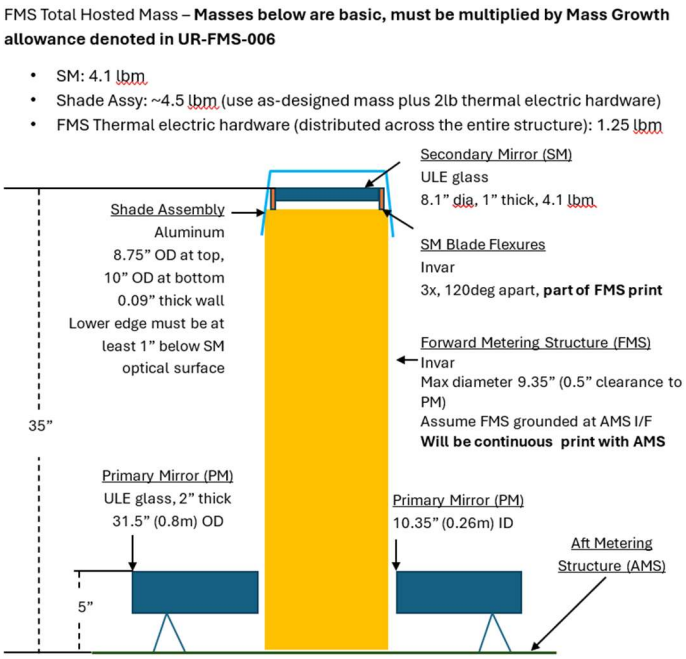

Figure 1. Mechanical Interface Control Drawing (MICD).

CONCEPTS

Leading up to the Preliminary Design Review (PDR), the design process involved creating approximately 20 initial computer-aided design (CAD) concepts to narrow down to a final, optimized selection. This phase was driven by a rigorous "fail-fast" technical feedback loop, in which designs that failed to meet the performance requirements outlined above were either dropped or improved. This process falls in line with the design philosophy presented by L3Harris: "Fast. Forward." The following three concept designs are the product and stand on the shoulders of numerous iterations and improvements.

1. Design A (Annex B, Figures 1 & 2) emerged from the idea of iterating upon pre-existing diamond lattices used in the additive manufacturing industry to create a structure with both high relative stiffness and low obscuration. The first 5 inches of the FMS below the PM did not contribute significantly to optical obscuration; this region could remain mostly solid to increase base stiffness. Significant mass reduction measures were taken by subtracting circular sections from the base of the FMS, and by eliminating the need for a top stiffening ring, allowing the SA and SM to both mount onto each of the three supports at the top of the FMS. The external diameter of the FMS was set to coincide with the edge of the design envelope (Figure 1) as preliminary calculations (Annex C, Figures 12 and 13) concluded that maximizing the overall diameter of the FMS would lead to a higher second area moment, and therefore, a higher overall stiffness per unit mass.

2. Design B (Annex B, Figures 3, 4 & 5) emerged from the idea of adapting existing triple bipod aerospace structures to create a structure with high stiffness, relatively low obscuration, and minimal material usage. Two smaller triangles were cut out of each of the bipods, maintaining overall stiffness while significantly reducing mass and obscuration. Like Design A, the base was a hollow tube with circular holes cut out to significantly reduce weight while sacrificing minimal stiffness. Due to the constrained nature of the FMS base, significant material could be removed from this region with minimal penalties to stress and first mode frequency. Most edges were rounded to ease stress concentrations in the middle of the FMS, and a small stiffening ring at the top was included to allow for mounting the SA offset by 60 degrees from the SM flexures. The distributed attachment points of the SA and SM were intended to reduce localized stress concentrations and improve overall load distribution. Additional small subtractions were made at the top and bottom of the structure to reduce mass and decrease obscuration at a minimal stress penalty. Like Design A, the overall diameter of the FMS also coincided with the external diameter of the design envelope to optimize stiffness.

3. Design C (Annex B, Figures 6 & 7) emerged from the idea of combining two triple bipod structures on top each other (converging on 6 nodes, 3 on the bottom of the FMS fixed to ground, and the other three on top underneath each flexure) and truss-like elements found in aircraft fuselages to both optimize for stiffness and stress distribution while minimizing the mass and obscuration significantly more than previous designs. First, to minimize lots of mass, while still utilizing the extreme stiffness provided by the SPC 123456 fixed constraint to the AMS at the bottom of the structure, the bottom 5 inches of the structure underneath the Primary Mirror consists of three 4-inch towers, each rotated about the center by 120 degrees, directly sitting underneath the direct load path from the flexures at the top of the structure. A 1-inch ring was added above the towers to transition the load path into two stacked triple-bipod sections, consisting of similar triangle sketches as Design B (with different dimensions). At 18.25 inches up the 33-inch FMS, the bipods are split by a cross-bracing ring to improve buckling resistance under angled loads. Now, this may have been causing some issues in terms of bending, but overall, it seemed like an interesting way to go. Overall, the main idea was to direct as much of the load path in three straight lines as efficiently as possible, while still opening unblocked space for the reflecting light from the PM to travel.

The three designs were evaluated in a two-stage selection process: a technical compliance screening and a comparative outlook. This process is exhibited in Table 1. In the first stage,

the three designs were first individually evaluated against six L3Harris technical specifications. It's important to note that none of the designs selected were able to meet all the rigorous specifications. However, this process showcased which design was the closest and could be improved to satisfy all constraints. The design that adhered to the most specifications was designated as the technical baseline. In the second stage, the three designs were compared against subjective metrics determined by the team. This included manufacturability, complexity, improvability, and design maturity. These four categories have been part of the team's thought process since the beginning of the project. The baseline design would compare against the other two in these categories, and the design with the highest cumulative performance would be selected as the design moving forward. This is a classic example of the down-selection methodology presented by L3Harris.

Ultimately, this process resulted in the team selecting Design B. This design met four out of six specifications and had the highest cumulative total across the subjective criteria. It did not, however, meet the mass specification (0.47 lbm over) [UR-FMS-006] nor the obscuration specification (11.73% over) [UR-FMS-020]. As a result, these metrics were given marginal status due to being close, with lots of room to improve using tools such as topology optimization.

At this point, the team would now work together to optimize this design and fabricate a prototype FMS for real-world testing to evaluate simulation accuracy.

From this point on, the team refined design B to comply with specifications [UR-FMS-006] and [UR-FMS-020]. This process is described in further detail in the analysis section. Additionally, an interface between the FMS and the SM using flexures was designed to meet these specifications.

The following three designs reflect important iterations of the entire design:

1. Design D (Annex B, Figure 8) emerged as a "best case" scenario to fulfill [UR-FMS-020]. Its obscuration is measured at 22.53%, only .53% over the required 22%. This drop in obscuration was made possible by cutting material from the FMS along light rays using the MATLAB script described in the analysis section. This design showcases the capability of the MATLAB script to optimize obscuration by cutting along the exact orientation that light flows. In the end, this design was scrapped because the light obscuration became of far less concern compared to the first mode, there were some important takeaways from this iteration. Primarily, the slots design and placement were adapted into a prominent part of many future iterations, as seen in weekly prints.

2. Design E (Annex B, Figure 9) was the first attempt at developing the FMS to SM interface. This design took the approach suggested by L3Harris, in having an uncomplicated three straight arm approach. While this design was unable to fulfill the yield and F.O.S requirement, it demonstrated a few key techniques that would be implemented in the final flexure design, such as including a surface completely flush to the SM, and the glue constraint to bind the SM to the flexure.

3. Design F (Annex B, Figure 10) was the first design to feature an approach modelling a thin piece of RTV that sat flush between the flexure and SM. The RTV allows simulation to closely reflect the real-world conditions of translation in the SM and flexures while preventing simulation artifacts present in earlier iterations, causing singularities and pressures to transmit force into the SM. This was another design feature that was present in the final design, with a few alterations. Additionally, it also made use of a spline to model the flexure arm, an addition that also limits simulation artifacts by eliminating sharp corners.

All iterations indicated important milestones in the design process, with features that showed relevance in later iterations and the final design. The philosophies present in the final design would not be possible without these initial designs.

Table 1. Two-Stage Selection Process (Phase 1)

	Preliminary Designs: Specifications		
CRITERIA	**A**	**B**	**C**
UR-FMS-001			
UR-FMS-002			
UR-FMS-003			
UR-FMS-006			
UR-FMS-007			
UR-FMS-020			

Legend	
	Compliant
	Marginal
	Not Compliant

Table 2. Two-Stage Selection Process (Phase 2)

	Preliminary Designs: Evaluation		
CRITERIA	**A**	**B**	**C**
Manufacturability	-1	0	0
Complexity	0	0	1
Improvability	-1	0	-2
Design Maturity	-2	0	-3
TOTAL	**-4**	**0**	**-4**

MECHANICAL ANALYSIS

The final iteration designed by the ME205 Senior Design Teams is acceptable and complies with five out of six specifications set forth by our sponsor, L3Harris. While, the sixth requirement, [UR-FMS-020], was not met due to a necessary trade-off between weight and performance, a formal waiver was granted

by L3Harris. A chart documenting the compliance is seen in Table 3. A convergence study (Table 3a) was conducted to ensure the validity of simulated values in Table 3. The final design and prototype can be seen in Annex E, Figures 6 and 7.

Table 3. Final Design Compliance

	Final Design: Specifications
CRITERIA	Design: 26c026607A
UR-FMS-001	Compliant
UR-FMS-002	Yield: 0.0127 > 0 Ultimate: 0.526 > 0 SM Ultimate: 0.390 > 0 Buckling: 7.23
UR-FMS-003	RSS: 7.10 µin RSS: 0.0108 µrad
UR-FMS-006	24.63 lbm
UR-FMS-007	61.82 Hz
UR-FMS-020	31.19%

Legend	
	Compliant
	Not Compliant

Table 3a. Final Design Convergence Study

Iteration	Mesh Size (in)	Max Stress (MPa)	%Change
1	0.4000	119.83	N/A
2	0.3000	115.81	3%
3	0.2000	118.50	2%

Max Displacement (in)	%Change
0.14	N/A
0.142	1%
0.144	1%

1. TOLERANCE ANALYSIS

A worst-case stack-up tolerance analysis was performed using the provided manufacturing tolerances for the SM and flexures using the setup shown in Annex C, Figure 9**.** The first case assumes the SM to be manufactured in its worst tolerance metric, and that the flexures be manufactured such that the distance between the SM and flexures is maximized. The second case assumes the SM and flexures to be manufactured with tolerances such that the distance between the two structures is minimized, covering both tolerance extremes. There is no literature outlining the application tolerance of RTV 566, but due to its gap-filling properties as an adhesive, it is assumed that small tolerance differences have a negligible effect on the overall assembly.

This is corroborated by the 0.040 $\frac{+0.00240}{-0.00201}$ inch worst case stack up tolerances, where the approximately 0.002-inch deviation is an order of magnitude smaller than the RTV's nominal thickness of 0.040 inches, which in addition to its adhesive properties, makes the calculated tolerances negligible in an assembly context.

2. FATIGUE ANALYSIS

In a temperature-controlled orbital environment, the FMS is expected to only experience a cyclical temperature load of 21±1°C according to the team at L3Harris. They also specified a mission length of 3 to 5 years, meaning that the FMS would have to at least survive the number of cycles within that time frame. Due to the loading and spring-like behavior of the flexures within the FMS during isothermal expansion, this would be the limiting component within the structure. To ensure compliance, the proposed strategy was to design the flexures such that they would have an infinite fatigue life.

The fatigue limit of Invar 36 in sheet specimens under consistent, cyclical loading was experimentally established to be between 27 ksi and 31 ksi [2]. These values were averaged to 29 ksi (199.95 MPa) for the following analysis. When subjected to the temperature load, the flexures experienced a maximum thermally induced stress of 9.644 MPa (Annex C, Figure 10), a value well under the fatigue limit.

The fatigue limit was also compared against the maximum von Mises stress experienced by the entire FMS during the quasi-static, combined launch load [UR-FMS-001]. The limiting stress factor [UR-FMS-002] is the yield factor of safety, meaning the entire structure can only experience up to 120 MPa under these loads (Annex C, Figure 4). It is worth noting that there is a significant margin between the maximum yield stress of the FMS and the fatigue limit of the material itself. This margin may account for manufacturing differences, material property differences, and other real-world inconsistencies that would lower the fatigue limit of the invar. Therefore, it is reasonable to conclude that the FMS will have an infinite fatigue life under both orbital and launch conditions, which represent both the minimum and maximum subcases.

3. FASTENER CALCULATION

The SA is secured to the top ring of the FMS via three #6-32 UNC through bolts spaced 120° apart, secured by nuts and washers (Annex C, Figures 1 and 2) to distribute the loads induced by the quasi-static launch loads over a wider area. The bolt preload and torque required were calculated as shown in Annex C, Figure 11.

The FEM setup was modified, adding fully fixed constraints to the edge of the bolt holes in the FMS to obtain an approximation of the reaction forces and moments that the bolt would experience. The maximum reaction force of 136.08 lbf and reaction moment 19.32 lbf•in were taken. The coefficient torque coefficient *K* was approximated to be 0.2, a value typical for unlubricated metals. The nominal diameter was taken to be

0.138 inches. It was found that the bolt preload must be 517.948 lbf given the tensile strength and tensile area of a standard SAE Grade 2 #6-32 bolt [36]. The resulting torque to install the bolt was then calculated to be 14.295 lbf•in given the 517.948 lbf preload. The preload lies well within the strength of standard #6-32 bolts, which range from 374 lbf to 817 lbf [2]. The required torque is also within reason, with standard #6-32 bolts needing a dry torque from 10 lbf•in up to 22 lbf•in [2].

4. COMPUTER BASED ANALYSIS

Computer-based simulations have been the driving force of this project. Siemens NX, NASTRAN, and MATLAB have been instrumental in guiding and verifying iterative design.

To verify [UR-FMS-020], MATLAB code had to be developed to read .csv files containing light ray geometry and check for an intersection against a .3mf file. This code was supplied to the team by L3Harris and instantly allowed for the obstruction percentage to be calculated, which guided design accordingly. However, the script's only output was displaying red or blue points on the PM that corresponded to the end of a light ray, meaning finding the correct angle to remove material required trial and error (Annex F). To streamline this workflow, modifications to this code were made so that it would move the intersected light rays and save them into a Python script. This script could be used with NX Open, allowing for light rays and their subsequent angles to be referenceable geometry in the part. This helped guide design around [UR-FMS-020], although the requirement could not be fully met.

To perform accurate Finite Element Analysis, the group had to value computation intensity against accuracy. A single FEM was used to run four simulations for requirements [UR-FMS-001] (SOL 101), [UR-FMS-002] (SOL 101 and SOL 105), [UR-FMS-003] (SOL 101), and [UR-FMS-007] (SOL 103). Typically, an FEM model would consist of a 3D mesh for the structure in its entirety. However, doing so for a structure of this size creates runtimes on the order of hours and results files over 20 GB due to the extra DOFs introduced by solid elements. While these simulations may be more accurate in nature, the group must consistently create a design, run a simulation, and then iterate on that design accordingly. With hours in between each simulation, this process becomes inefficient, and with a time frame of just over 3 months, it also becomes a detriment to meeting these requirements.

To circumvent our computational limitations, certain techniques are performed on the model to cut simulation time down without harming the results. Firstly, the entire FMS, except for the flexures, is midsurfaced by face pairs using an idealized part. This allows a 2D mesh to be used in place of a 3D mesh, significantly reducing the number of elements to compute. The flexures, RTV, and SM are all separate 3D meshes. The flexures are connected to the FMS by face-to-face RBE2s, which simulate the connected nature of the two bodies at that interface. The material properties for RTV 566 were obtained from Matweb [12] and the material properties for the ULE 7972 used for the SM are from the supplied reference document from Corning. The SA interfaces with the FMS through a 0D lumped mass with inertial properties connected by RBE3 elements to the bolt holes on the FMS around a simulated washer diameter (Annex C, Figure 2). This was done to simulate the mass and bolted connection without giving the SA any stiffness, as it is not a valid load path. The bulk density of the SA was also calculated to include the geometry (Al_6061) as well as the 2.5 lbm of hosted thermal electric hardware.

In the SIM setup, six separate surface-to-surface glue connections are used to connect the flexure to the RTV, and RTV to the SM to simulate the stiffness and adhesive properties of the RTV while minimizing artificial stiffness. An SPC 123456 is applied to the bottom of the FMS. Since the FMS is printed on top of the AMS print as one large piece [UR-FMS-012], it's fully fixed at that edge. Additionally, a nonstructural mass (NSM) is applied by distributing 1.25 lbm of thermal electrical hardware specified in the MICD (Figure 1) over the surface area of the FMS structure, excluding the flexures.

To validate the yield and ultimate margins of safety [UR-FMS-001] and [UR-FMS-002], a SOL 101: Linear Statics solution was created to run 266 subcases that composed a 30g spherical sweep, incremented by 15° combined with a 5°C to 35°C thermal load with a stress-free temperature of 21°C. This was accomplished using .inc files to define all 266 subcases and gravity loads. Manually editing the .dat file allowed for this inclusion before submitting it to Nastran directly for solving. The maximum von Mises stress for the FMS, flexures, and SM were identified and the margins calculated (Annex C, Figure 4). Specifically, von Mises was used to calculate the yield MOS, and the max principal stress was used to calculate the ultimate FOS. Throughout the design process, there is a positive correlation between the removal of mass from the top of the FMS and the decrease in overall stress experienced by the structure. To validate the buckling FOS, a SOL 105: Linear Buckling solution was created to evaluate the smallest, first positive eigenvalue under the same loads and constraints (Annex C, Figure 5).

To validate [UR-FMS-003], a SOL 101: Linear Statics solution was created with a 1°C isothermal temperature change from a reference temperature of 20°C as the average temperature between 5°C and 35°C. A temperature load of 21°C was applied, and the nodal displacements of the SM were evaluated. The FEM and idealized part were then edited such that the SM was a midsurface with 0.2in CQUAD4 elements, then glued back to the assembly in the SIM as previously described. This was done to find the rotational displacement of the SM, as 3D solid elements do not have rotational DOFs. Like the nodal displacements, these values were calculated in an RSS to validate their compliance with [UR-FMS-003].

To validate [UR-FMS-007], a SOL 103: Real Eigenvalues solution was created to evaluate the modal response of the FMS. Maximizing the first mode was found to be highly dependent on shortening vertical members and distributing mass lower down the structure. This was quantified using strain energy density, and areas of high strain energy density had material added to increase the local stiffness. Material was found to be most effective at the base, as lightening the base had positive effects on the mass budget, but drastic effects on the first mode without additional reinforcement. The resultant first mode was 61.82 Hz (Annex C, Figure 7).

To verify [UR-FMS-020], MATLAB code had to be developed to read .csv files containing light ray geometry and check for an intersection against a .3mf file. This code was supplied to the team by L3Harris and instantly allowed for obstruction percentage to be calculated. The final obstruction came out to 31.19% (Annex C, Figure 8) using a high-definition ray bundle.

5. MATERIAL SELECTION

[UR-FMS-005] specifies that the FMS material shall be Invar (or an Invar-class alloy) to minimize coefficient of thermal expansion (CTE) driven misalignment. This directly affects [UR-FMS-001], [UR-FMS-002], and most notably [UR-FMS-003], as Invar's low CTE allows for thermal loading to have submicron displacement effects. While other materials such as tungsten may fill this requirement, the team settled on invar as working with given values eliminates time spent on material property research.

L3Harris requests we assume the following nominal values of the material to be listed in Table 4. Additionally, the SM is specified to have the material properties of Corning ULE 7972, as defined by Corning with relevant properties listed in Table 5. Additionally, the team discussed the adhesive typically used to connect the SM and FMS, where RTV 566 was declared to be used. As such, the team found values for RTV 566 on Matweb for use in simulation. Since MatWeb had a range from 54 µm/m·°C to 340 µm/m·°C with an average of 247 µm/m·°C (Table 6), a study was conducted to determine the maximum CTE before [UR-FMS-003] was no longer compliant. Through simulation, it was found that the CTE for the RTV can be no larger than approximately 150 µm/m·°C, which falls into the CTE range given for the RTV.

Table 4. Material Properties of Invar

Property	Value
Density	8.10 g/cm³
Coefficient of Thermal Expansion (CTE)	0.4 ppm/°F
Young's Modulus	141 GPa
Poisson's Ratio	0.29
Yield Strength	240 MPa (34.8 ksi)
Ultimate Tensile Strength	500 MPa (72.5 ksi)
Thermal Conductivity	10 W/m·K
Specific Heat Capacity	515 J/kg·K
Electrical Resistivity	0.78 µΩ·m at 20°C
Magnetic Permeability	100 (relative to vacuum)

Table 5. Material Properties of ULE glass from Corning

Property	Value
Density	2.21 g/cm³
Coefficient of Thermal Expansion (CTE)	0 ± 30 ppb/°C (5°C–35°C)
Young's Modulus	67.6 GPa
Poisson's Ratio	0.17
Ultimate Tensile Strength	49.8 MPa (7220 psi)
Shear Modulus	29.0 GPa
Bulk Modulus	34.1 GPa
Thermal Conductivity	1.31 W/m·K
Specific Heat Capacity	767 J/kg·°C
Thermal Diffusivity	0.0079 cm²/s
Electrical Resistivity	$10^{11.6}$ ohm·cm (at 200°C, 100 Hz)

Table 6. Material Properties of RTV 566 from MatWeb

Property	Value (Metric)
Density	1.27 g/cm³ (avg)
Coefficient of Thermal Expansion (CTE)	247 µm/m·°C (avg)
Young's Modulus	0.0481 GPa (avg)
Tensile Strength	5.41 MPa (avg)
Shear Strength	0.617 MPa (avg)
Thermal Conductivity	0.777 W/m·K (avg)
Specific Heat Capacity	1.46 J/g·°C

6. FUNDAMENTAL MECHANICAL ANALYSIS

The mechanical analysis of the Final Design was done in a similar process to the Preliminary Design. To support early concept direction with objective metrics, the team opted to complete two preliminary "one-pager" analyses that document assumptions. The first analysis establishes a circular, hollow tube baseline within our design envelope to quantify how stiffness (axial/bending/torsion) and weight scale with wall thickness, providing a reference stiffness-to-weight trade for evaluating candidate FMS concepts. The second evaluates thermal sensitivity under a 1°C isothermal change and estimates allowable temperature non-uniformity between Secondary Mirror flexure supports to satisfy [UR-FMS-003] rotation and translation requirements, reinforcing the design need for symmetry and thermal uniformity. These one-pagers can be found in Figures 10,11, and 12 in Appendix C.

While developing the FMS – SM interface, a key consideration was the thickness of potential flexures. To ensure minimal load transfer to the SM, low stiffness was desired. With a smaller thickness, the team could lower the stiffness of the flexures, allowing the members to deflect instead of remaining rigid and transferring stress in the SM. To start, the group began simple hand calculations, seen in Annex F, using MATLAB of a cantilever beam to determine the minimum thickness required to fulfill [UR-FMS-002] and [UR-FMS-003]. These showed a minimum thickness requirement of 0.138 inches. This helped guide design from simple straight members, which eventually transformed into more complex spline-based geometries.

MANUFACTURING

As introduced in the problem statement, the purpose of this project was to design and fabricate a forward metering structure (FMS) for a Cassegrain-style optical satellite system. The FMS is responsible for connecting the primary mirror assembly to the secondary mirror assembly while maintaining optical alignment through relevant structural and thermal loading environments. Because the FMS directly affects optical alignment, manufacturing was not treated as a secondary design concern. Instead, the manufacturing process was one of the central drivers of the project.

A key objective from L3Harris was to explore a design optimized for additive manufacturing, specifically metal additive manufacturing using Direct Metal Laser Sintering (DMLS). DMLS, also commonly discussed under the broader category of metal laser powder bed fusion, fabricates parts by spreading thin layers of metal powder and selectively melting

or sintering each layer with a high-power laser before lowering the build platform and repeating the process layer by layer [4]. This process is valuable for aerospace structures because it can produce complex geometries, consolidate multiple components into a single part, reduce assembly operations, and support low-volume production without the tooling burden associated with traditional manufacturing [5].

For this project, the speed and flexibility of DMLS were especially important. A subtractive-manufactured FMS would likely require multiple manufactured components, fasteners, joining operations, and inspection steps. Each additional interface would introduce a tolerance stack-up and potential alignment error. In contrast, a monolithic additively manufactured FMS could reduce part count, simplify assembly, and better preserve the intended relationship between the primary and secondary mirror interfaces. This is particularly important for an optical metering structure, where small dimensional errors can affect the final optical alignment.

The manufacturing approach, therefore, had two connected purposes. First, the final CAD design needed to demonstrate geometry that could reasonably be produced by metal additive manufacturing. Second, the physical prototype needed to represent the full-scale design well enough to support design day demonstration, assembly understanding, and manufacturing feasibility discussion within the limits of the team's budget, schedule, and available equipment.

1. ORIGINAL MANUFACTURING INTENT

The original manufacturing concept was to produce the FMS as a single monolithic metal additively manufactured part. The target material for the intended final design was Invar 36 because of its low coefficient of thermal expansion and use in applications requiring high dimensional stability. Stephenson et al. identify Fe-36Ni alloys as materials of choice for low coefficient of thermal expansion applications, especially optical, instrument, and electrical systems where dimensional stability is critical [6]. Wei et al. also discuss the additive manufacturing of Invar 36 by selective laser melting and identify the alloy's low thermal expansion behavior as a major reason for its use in precision and aerospace applications [7].

In a space-based optical system, thermal stability is critical because small dimensional changes can lead to misalignment between the primary and secondary mirrors. A monolithic Invar 36 DMLS structure would help reduce thermal distortion while also eliminating many mechanical joints that could introduce tolerance stack-up, loosening, or assembly error. Although Invar 36 was used as the intended material for the final design and analysis work, it was quickly ruled out for the physical prototype because of cost and availability. Invar is a specialty alloy, and printing a large student prototype in Invar through an external DMLS vendor was not realistic within the project budget. As a result, the team investigated lower-cost metal alternatives, especially aluminum alloys, for either a full-scale or reduced-scale prototype.

The design was also intended to be printed vertically. A vertical orientation was preferred because it better represented the final structure as one continuous metering assembly and supported the broader project goal of producing an integrated additively manufactured structure. In a future production version, this vertical build concept could also support integration with the aft metering structure (AMS) in a larger single-build architecture. The vertical print strategy also influenced design decisions related to support material, overhangs, access for post-processing, and preservation of critical interface regions. These considerations are standard design-for-additive-manufacturing concerns, since build orientation, support strategy, overhangs, residual stress, and post-processing all strongly affect final part quality in metal additive manufacturing [8,9].

However, the size and cost of a full metal DMLS prototype quickly became major constraints. The FMS is long, thin, and relatively large compared with typical student project prints. A full-scale metal version would require a printer with sufficient build volume, compatible metal powder, stress-relief or heat-treatment capability, support-removal access, and post-processing options for cleaning up interface surfaces. Residual stress and distortion are known limitations in metal additive manufacturing, and they often require careful process planning, support design, and post-build heat treatment or stress relief [9]. These specialized industrial capabilities were not available on campus and were expensive through external vendors, so the team investigated outsourcing options early in the manufacturing phase.

2. VENDOR INQUIRIES AND MANUFACTURING TRADEOFFS

Due to the size and complexity of the FMS, the team contacted several external manufacturing vendors to evaluate whether an outsourced metal additive prototype was practical. These vendors included Xometry, Baker Industries, Protolabs, and Craftcloud. Xometry, Baker Industries, and Protolabs were useful early points of contact, but each option was eventually eliminated because the part could not be produced within the team's budget, could not be delivered within the required time window, or exceeded the physical capabilities of the specific machines and processes available through that vendor. These discussions helped confirm that the FMS was not a simple quote-and-print part. Its full-scale height, preferred vertical build orientation, thin structural members, and aerospace-style geometry made the print difficult to manufacture without reducing scale, sectioning the part, changing material, or accepting high cost and schedule risk.

Craftcloud became the most developed vendor discussion because they were able to provide multiple manual quotes through their manufacturing network. The team initially inquired about aluminum AlSi10Mg as a lower-cost alternative to the sponsor's intended Invar 36 material. The original request asked for a single vertically printed metal part, with a target budget of approximately $1,000 and a required delivery window of roughly four to five weeks. After reviewing the CAD model, Craftcloud provided manual SLM aluminum quotes for several scales. The quoted production and welding costs were approximately $2,870 for a 100% scale print, $1,225 for a 75% scale print, and $345 for a 50% scale print. Shipping was quoted separately at approximately $280, $205, and $125, respectively. The stated production lead time was 12 working

days, with an additional 5–8 working days for shipping. The quote also noted that the part would need to be separated and welded together, with possible welding deformation of approximately 1–2 mm and expected tolerance between 0.3 and 1.0 mm.

These details showed that even the most promising metal-printing option did not fully match the project's original manufacturing intent. A full-scale aluminum print exceeded the available budget, and the need to separate and weld the part conflicted with the intention to demonstrate a monolithic additively manufactured FMS. The welding deformation and tolerance range were also concerning because the FMS is fundamentally an alignment-sensitive structure. After the design was updated, the team requested another Craftcloud quote focused on the largest aluminum print that could fit within the remaining budget of approximately $800, along with confirmation of vertical print orientation, lead time, and vendor location. Craftcloud later confirmed that the updated geometry could be printed vertically in SLM aluminum, but the one-piece option was significantly reduced in scale, with a production cost of approximately $190, shipping of approximately $115, a 10-business-day production lead time, and 5–8 business days for shipping.

Ultimately, the team decided not to proceed with Craftcloud or another external vendor. The primary issue was not only cost but also a lack of control. Outsourcing the print would have limited the team's ability to control print orientation, inspect the part during manufacturing, communicate directly with the machine operator, respond quickly to geometry issues, and guarantee delivery before the final project deadline. This concern was reinforced by feedback from previous senior design teams, who had reported issues with outsourced prints, including delays and lower-than-expected print quality. Based on these risks, the team determined that a locally produced, full-scale, sectioned ABS prototype would better support the final project goals than a smaller outsourced metal print.

Table 7. Craftcloud Quote Summary

Craftcloud Quote Option	Production Cost	Shipping Cost	Lead Time
100% Scale	$2,870	$280	20 days
75 % Scale	$1,225	$205	20 days
50% Scale	$345	$125	20 days

3. ITERATIVE PROTOTYPE MANUFACTURING

Throughout the design process, the team used rapid prototyping to evaluate geometry before committing to a final full-scale print. Weekly prototype prints were produced at approximately 48% scale using a teammate's personal 3D printer. These prints were not intended to validate structural performance. Instead, they were used as design development tools to evaluate manufacturability, geometry, handling, and assembly risk.

The reduced-scale prototypes helped the team evaluate whether the FMS geometry was physically understandable and buildable, whether the support legs and ring features were too thin or fragile, whether the design appeared too closed off from an optical-obscuration standpoint, whether the structure could be handled without breaking, and whether sectioning or print-orientation changes would be needed for the final prototype. These prints were especially useful because several features that appeared reasonable in CAD were difficult to judge without a physical model. The prototypes helped expose practical issues related to thin members, printability, support placement, access, and assembly. They also allowed the team to communicate design changes more clearly during internal team discussions, L3Harris reviews, and advisor meetings.

4. FINAL PROTOTYPE MANUFACTURING APPROACH

The final manufacturing approach was to produce a full-scale representative FMS prototype using 100% infill ABS on a Stratasys F270 printer. The Stratasys F270 is part of the F123 series of FDM printers and uses GrabCAD Print software for print preparation. The available F270 build volume is 12 in × 10 in × 12 in, which was insufficient to print the approximately 33-inch-tall FMS as one continuous part [10,11]. Because the full-scale structure exceeded the available printer volume, the final prototype was divided into multiple sections, printed separately, and bonded together using epoxy.

The sectioned approach was selected to preserve full-scale geometry while staying within the printer's build-volume limits. To improve alignment during assembly, holes were added at the section interfaces, and 0.1-inch ABS dowels were printed and used as datum/alignment features. These dowels helped locate the sections relative to one another during bonding and reduced the risk of visible mismatch between printed segments. Although this approach introduced joints that would not exist in the intended monolithic DMLS design, it allowed the team to produce a full-scale physical model that accurately represented the design envelope, major load paths, interface locations, and optical openness of the final FMS concept.

The use of 100% infill ABS was selected to improve handling, durability, and stiffness compared with a lower-infill polymer print. The prototype was expected to be handled, transported, assembled, and displayed, so durability was more important than reducing polymer material usage. The Stratasys F123 platform supports ABS materials and soluble support material for complex FDM prototypes [11]. ABS does not match the stiffness, strength, density, or thermal expansion behavior of Invar 36, so the prototype should not be treated as a flight-like structural test article. However, it was appropriate for a full-scale geometric prototype and could still be represented in simulation by assigning ABS material properties and applying test-representative boundary conditions.

The final print process was supported in large part by Jim Alkins, who provided access to the printer and assisted with print planning, troubleshooting, post-processing, and part storage. This local manufacturing support was a major reason the team selected the in-house ABS route over an outsourced metal print.

5. FINAL PROTOTYPE PRINT TIME AND MATERIAL USAGE

The final full-scale prototype required multiple print jobs because the FMS was divided into separate sections. GrabCAD Print estimates were used to record print time, ABS material usage, and QSR support material usage for each section. These values were important for estimating manufacturing cost and understanding the practical time commitment required to produce the full-scale prototype. While the ABS prototype was not equivalent to the intended DMLS Invar structure, the print-time and material data provided a realistic manufacturing estimate for the physical system delivered by the team.

Table 8. Final ABS prototype print estimates

Section	Print Time	ABS Material	QSR Support Material
6	17 hr 41 min	16.028 in³	7.366 in³
5	16 hr 1 min	16.498 in³	3.466 in³
4	18 hr 7 min	16.238 in³	5.506 in³
3	7 hr 25 min	5.54 in³	3.828 in³
2	9 hr 49 min	10.143 in³	4.046 in³
1	10 hr 1 min	9.345 in³	4.273 in³
Subtotal	**79 hr 4 min**	**73.792 in³**	**28.485 in³**

The values in Table 8 represent the print sections available at the time of documentation. If additional sections are printed or reprinted, the final manufacturing cost estimate should be updated accordingly.

6. COST ESTIMATE

The assignment requires manufacturing cost to include purchased hardware cost, purchased shop time if applicable, and team member manufacturing time costing at $100/hr. Development time should be reported separately and should not be included in the prototype build cost. For this project, the manufacturing cost estimate includes printed ABS material, support material, epoxy, printed alignment dowels, shop/printer time if billed, and team labor for print preparation, support removal, section fit-up, bonding, post-processing, and final assembly (Table 9).

Table 9. Final Total Manufacturing Cost Estimate

Cost Item	Quantity / Basis	Unit Cost	Estimated Cost
ABS Model Material	73.792 in³	$3.75 / in³	$276.72
QSR Support Material	28.485 in³	$3.80 / in³	$108.24
Alignment Dowels	0.0141 in³	$3.80 / in³	$0.05
Purchased Shop Time	81.067 hr	$100 / hr	$8006.70
Team Labor (slicing, communication with shop, and assembly)	6.0 hr	$100 / hr	$600
Total	**N/A**	**N/A**	**$8991.71**

7. SCALING TO 1000 SYSTEMS

If this system were scaled to 1000 units, the manufacturing process would need to shift from student prototype fabrication to a controlled production process. The final production design would likely return to the original intent of a monolithic DMLS metal structure, most likely using Invar 36 or another thermally stable alloy approved by the customer. At that scale, the largest improvements in cost and build time would come from process standardization rather than changing the basic function of the structure.

Several changes could improve manufacturability at a larger scale. The design could be further optimized to reduce support material, improve powder removal, simplify post-processing access, and add consistent machining allowances at critical interfaces. Build orientation and support strategy could be standardized after qualification testing. Inspection fixtures could also be developed to measure the secondary mirror interface relative to the primary mirror or AMS datums. Since residual stress and distortion are important concerns in metal additive manufacturing, a production process would also need defined stress-relief procedures, inspection requirements, and acceptance criteria [9].

Although DMLS would remain more expensive than polymer printing or simple machining, its value for this application is the ability to produce a complex integrated metering structure with fewer parts and fewer assembly operations. For an optical alignment structure, reducing part count, tolerance stack-up, and assembly labor may be more important than minimizing raw material cost alone. In a 1000-system production case, cost reduction would likely come from standardized build layouts, qualified process parameters, repeatable post-processing, reduced manual finishing, and dedicated inspection tooling.

Overall, manufacturing was not just the final build step of this project. It directly shaped the design, vendor decisions, prototype strategy, and final deliverable. The intended manufacturing approach was a monolithic DMLS Invar 36 structure, consistent with the sponsor's long-term goal of rapid additive manufacturing for precision aerospace hardware. However, due to budget, schedule, and equipment constraints, the team produced a full-scale sectioned ABS prototype using the Stratasys F270. This approach preserved the overall geometry and design intent while avoiding the cost, schedule risk, and lack of control associated with outsourced metal printing. The final prototype, therefore, served as a practical full-scale demonstration of the FMS concept, while the CAD

and analysis work remained tied to the intended DMLS metal design.

TESTING AND RESULTS

1. MATERIAL TESTING

A significant portion of this project was dedicated towards material testing to validate the performance of the FMS prior to manufacturing. However, while the FMS is designed to be manufactured via Direct Metal Laser Sintering (DMLS), a specific type of Powder Bed Fusion (PBF) additive manufacturing technology, using Invar 36, the team was unable to acquire relevant samples due to budget and timing constraints. In addition, the PBF process is not always consistent; in fact, each print introduces unique microstructural variabilities. Due to these issues, the team performed testing on a subtractive manufactured sample of Invar. It's important to note that the team recognizes that these tests don't exactly mirror PBF data. Instead, the objective of these tests was to cover a framework that demonstrates how these evaluations would be conducted to validate material.

Two tests were conducted: a 3-point-bend and a coefficient of thermal expansion (CTE) test. These specific tests were selected because they could be performed using identical specimen dimensions, which would make the manufacturing and preparation process much easier. Additionally, these tests targeted the performance metrics most critical to the FMS design.

The team began this study by consulting with Senior Technical Associate, Christine Pratt, who provided the necessary guidance throughout this testing process. Based on her equipment, the samples needed to be a rectangular prism with a length of 50 mm and a cross-sectional area small enough to fit within an 8 mm diameter. Since the raw stock of Invar provided by Professor Muir was significantly larger than these dimensions, the team met once again with Jim Alkins to cut the material using a band saw equipped with a carbide blade. The two cut specimens were then finished on a mill to ensure they were parallel.

For the 3-point-bend, the sample was loaded into a material tests system (MTS) machine centered across two support pins (Annex D, Figure 1). Once fixed on both ends, the machine applied a vertical compressive force, deflecting the prism over an increasing load. The specimen deflected a total of 0.15 inches at approximately 600 lbf (Annex D, Figure 2). To validate these experimental findings, a CAD part was modeled in NX [13] using material properties from MatWeb [12] and the same dimensions as the experimental specimen. The simulation was created with identical boundary conditions and four different compressive loads (Annex D, Figure 3). A comparative analysis was conducted using MATLAB [14] as shown in Figure 2. Ultimately this correlation proves that the team's engineering tools are correctly calibrated, which suggests that the existing simulations on the FMS are likely accurate reflections of how the real print will perform in space.

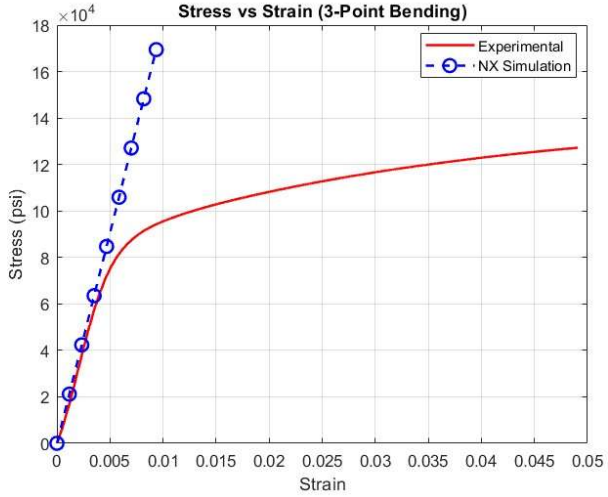

Figure 2. Comparative analysis: experimental vs simulated data.

Next a CTE test was performed using the second cut specimen. The original plan for this test was to utilize a specific oven with an integrated displacement sensor. However, upon preparation, it was discovered that several coils and wiring were faulty, preventing the oven from heating up. As a result, the team had to improvise with a makeshift test rig consisting of a separate furnace and external displacement meter (Annex D, Figures 4 & 5). Because this test system was not digitally synchronized, the data acquired would not be as precise. To account for these limitations, the team decided to test an aluminum sample alongside the invar. Since both tests would be administered under identical conditions, it would allow the team to generate a comparison profile as shown in Figure 3.

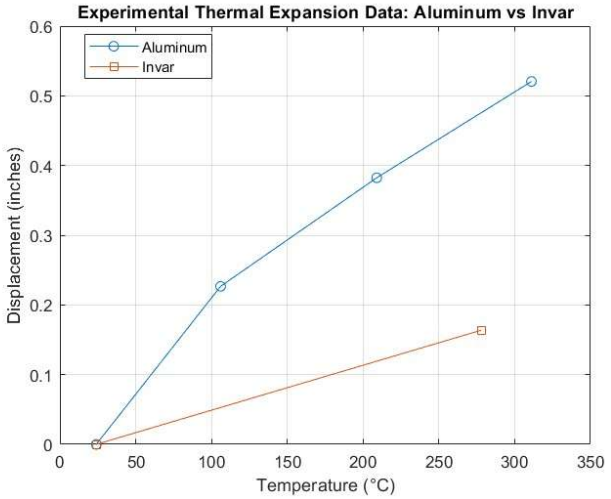

Figure 3. Thermal expansion data for aluminum and invar.

The values collected for aluminum corroborated with literature values found on MatWeb, which proved that the makeshift rig could measure CTE. However, the values for invar did not align with literature. This discrepancy was due to the limitations of the external sensor, which read erratic displacement values that were physically impossible. For this reason, the team was forced to filter the dataset. Yet, the results still proved that invar expands significantly less than aluminum. This is because Invar 36 experiences a phenomenon known as

the Invar Effect, which essentially is when atomic vibration and magnetic contraction work against each other [15]. This is why invar, "a name that derives from the word invariable," is selected for high precision applications [15].

In addition to the FMS manufactured out of Invar 36, the team wished to examine ZERODUR, a type of ultra-low expansion (ULE) glass like what would be used for the primary and secondary mirrors. Thanks to Ed Herger and the Optics department, several samples of ZERODUR were acquired for testing. However, since glass is transparent, an interferometry experiment would need to be conducted. That means that a laser would need to be split into a reference beam and a measurement beam while heated. If the peaks of the two beams no longer align, it would be clear that the glass sample expanded. After consulting with Ed Herger, it was agreed that this study would be too complex and out-of-scope with the original testing plan. Instead, this would be an application for future work.

2. PROTOTYPE TESTING

In addition to material testing, a vibration test was performed on the 3D printed physical prototype. The purpose behind this experiment would be to compare and validate the behavior of the physical 3D print with results found from NASTRAN FEA simulations, as requested by L3Harris.

The test was performed by suspending the FMS horizontally by three bungee cords. An accelerometer was placed on a part of the FMS with beeswax, and then tapped on a separate part with a calibrated force hammer (Annex D, Figure 9). From these tests, a first mode of frequency of 46.5 Hz was found (Annex D, Figure 10).

To correlate this test data to simulation data, ABS's mechanical properties were used. For density, the physical prototype was weighed and had an experimental density of 0.971 g/cm^3, then the simulation's density was updated to match this value. A SOL 103: Real Eigenvalues simulation was set up using the same configuration as previous simulations, but had free-free constraints instead to accurately model the test setup. The 1st mode of the simulation was 45.56 Hz (Annex D, Figure 11), only 2% error from the physical test. This is a very strong correlation and validates the assumptions made during the overall mechanical analysis of this structure.

There are small errors between the simulation and physical model, which can be accounted for by differences in the physical 3D printed model. While full-scale, the ABS FMS is a non-monolithic assembly with gap-filler glue, and contains sections printed in different orientations, which may potentially have caused discrepancies in test results when compared to simulation. The 2D shell model also does not fully match the volume of the actual 3D model, as the edge blends are not included in the FEM idealization.

INTELLECTUAL PROPERTY

Based on the patent research that was completed, the broad idea of a forward metering structure for a Cassegrain-style optical system is not new, since almost all similar telescope support and metering concepts already exist in prior art, and almost all optical systems of this kind require some form of metering structure to maintain alignment between optical elements. One strong example is US10534165B1, Athermal Cassegrain Telescope, which describes a Cassegrain telescope using a silicon-carbide telescope metering tube to maintain the relationship between the primary and secondary optics under thermal change [16]. Another relevant example is Raytheon's EP3356873B1, High-Stiffness Structure for Larger Aperture Telescope, which claims a telescope support assembly built around a metering structure with side beams, end pieces, and mirror-supporting struts [17]. These patents show that the general function of a thermally stable telescope metering structure is already well established in the patent space [16,17].

At the same time, the team believes that the project may still contain narrower novel elements in the specific way the structure is being designed and fabricated. Many existing examples are manually manufactured, assembled from multiple parts, or developed at very different scales. In contrast, this design is driven by a very tight cylindrical envelope and an additive-manufacturing-first approach. The structure is intended as a monolithic metal part, built in a vertical single-build orientation, while also remaining as open as possible to reduce light obscuration. This means that the likely novelty of the project does not come from the general purpose of supporting and spacing telescope optics. Instead, it comes from the exact way multiple difficult constraints are combined into one repeatable design.

Those constraints include not only stiffness and thermal stability, but also manufacturability, reduced assembly complexity, optical openness, and the ability to fabricate the structure as a single integrated build. This distinction is important because it changes how the patent potential of the project should be viewed. A broad claim on a general telescope metering structure would likely overlap heavily with existing work and would be difficult to defend. A narrower claim tied to a specific additive-manufacturing-driven geometry, a monolithic AMS/FMS integration strategy, or an obscuration-conscious structural load path within a narrow cylindrical package is much more realistic. The overall system function is not new, but there is a reasonable possibility that the exact implementation may be.

This also appears to be an active and competitive intellectual property space. L3Harris states that it designs and integrates precision optical telescope systems and metrology hardware for major space observatories such as the James Webb Space Telescope [18]. Northrop Grumman likewise highlights silicon-carbide material systems suitable for optical, structural, and metering applications in precision space systems [19]. ESA and Airbus have also documented thermally stable silicon-carbide and C/SiC optical structures for space telescope applications, including Herschel and Euclid [20–22]. This reinforces that the project is not entering an untouched field. Instead, it sits in an established technical area where major aerospace organizations are already developing high-performance optical structural systems for space applications [18–22].

Overall, the team concludes that the project is more likely to offer a narrow patent opportunity than a broad one. A general claim on a telescope metering structure would likely overlap

with too much prior art, but a more specific claim tied to the structure's additive-manufacturing-driven geometry, AMS/FMS integration, or obscuration-conscious load path design may be more realistic. The overall system function is already established, but the team's specific implementation and design may still be novel. At minimum, the project clearly occupies an active and competitive intellectual property space, and the design process demonstrates how additive manufacturing may open new structural solutions for future space optical systems.

SOCIETAL, ENVIRONMENTAL, AND ECONOMIC IMPLICATIONS

This project supports a class of space-based optical systems that has a meaningful impact on everyday civilian life, even if most people never directly see the hardware itself. Optical and remote-sensing satellite systems contribute to weather forecasting, disaster monitoring, environmental tracking, agricultural planning, and other space-based services that modern society depends on [23–26]. GPS is one major example, since it supports transportation, communications, positioning, navigation, and timing across critical infrastructure [27]. Weather and Earth-observing satellites also play major roles in storm tracking, wildfire monitoring, flood mapping, drought analysis, and resource planning [23,24]. In that sense, a project like this contributes indirectly to technologies that improve public safety, economic resilience, and overall quality of life.

From a public welfare standpoint, the value of this type of project is strongly tied to reliability and performance. A forward metering structure is not a consumer-facing product, but it helps enable the structural and thermal stability required for precise optical alignment in demanding space environments. If systems like these perform well, they support better data quality, more reliable observations, and more effective use of the satellite-based services that people rely on every day. This includes more accurate weather forecasts, stronger hazard response, better agricultural decision-making, and more dependable timing and positioning services across communications and infrastructure [23–27]. Because of that, even a structural subsystem like this has an indirect but meaningful connection to public health, safety, and welfare.

There are also broader social and global implications tied to this type of technology. Space-based optical systems help governments, researchers, and commercial organizations better understand conditions on Earth over large regions and long time periods. That has value not only in the United States, but globally, especially in areas such as food security, climate monitoring, storm prediction, and disaster response [23–26]. Satellite data is an important tool for tracking crop conditions, flood and drought impacts, wildfire damage, and ecosystem change [23–26]. Because of that, technologies that improve the manufacturability and repeatability of space optical structures can contribute, even indirectly, to more informed decision-making at both national and international levels.

Economically, the project is especially significant because one of its main goals is to improve manufacturability, reduce build time, and simplify production through metal additive manufacturing. On a part-by-part basis, this approach can still be expensive. Metal powder-bed fusion relies on specialized machines, carefully controlled processes, and costly feedstock materials [28–31]. Even so, for a company such as L3Harris, the long-term economic value is not limited to raw per-part print cost. The larger benefit comes from reduced part count, lower assembly complexity, less manual labor, faster design iteration, and the possibility of producing a repeatable monolithic structure in a single build rather than through a more complex multi-component manufacturing and assembly chain [29–32]. That type of approach becomes increasingly valuable when customers require high-performance hardware on shorter timelines and, potentially, in larger quantities.

There are also wider economic benefits associated with the downstream services enabled by systems like this. GPS timing supports communications systems, power grids, financial networks, and other critical infrastructure [27]. Earth-observing satellites support decision-making in agriculture, disaster planning, and resource management [23–26]. Even though this project is focused on one structural subsystem, it fits into a much larger economic picture in which more manufacturable and repeatable space hardware can support services that affect industries across the broader economy.

From an environmental perspective, there are both benefits and drawbacks to the approach being taken. The main drawbacks come from metal additive manufacturing itself, since powder-bed fusion is energy-intensive and depends on specialized feedstock, tight process control, and post-processing steps [28,30–32]. There is also an environmental cost associated with powder production, failed builds, support material, and any secondary machining or heat treatment required after printing [30–33]. At the same time, additive manufacturing can offer environmental advantages when it reduces part count, eliminates unnecessary assembly steps, avoids excess material usage, and allows the structure to be optimized more directly for mass and function [31,32]. In this case, designing a monolithic part instead of a more manually assembled structure may reduce manufacturing complexity and repeated handling, even if the printing process itself is not inherently low energy.

Several changes and optimizations could improve the environmental and overall efficiency footprint of a project like this. The design can be optimized to minimize support structures and reduce unnecessary printed mass. The geometry can also be shaped to avoid trapped powder regions and make powder removal easier, which would improve both cleanliness and material recovery. In addition, reducing post-processing demands through smarter build orientation and more print-ready geometry could lower total labor and energy input. Continued improvement in process control and model correlation could also reduce failed prints and rework, improving both economic and environmental performance [28,30–32]. Overall, while metal additive manufacturing has clear energy and material costs, this project is aimed at showing that a well-designed monolithic structure can still offer strong societal and economic value by enabling faster, more repeatable, and potentially more scalable production of high-performance space optical hardware.

RECOMMENDATIONS FOR FUTURE WORK

While obscuration was a large consideration in the design process from the project's inception, the final design fails the obscuration requirement by over 8%. While the requirement is likely possible to meet, it would likely require large amounts of finetuning, optimization, and redesign. With more time, the team could likely meet this requirement with continued use of the developed MATLAB code combined with NX optimization.

Additionally, all future work should see the design lean into its method of manufacturing. Additive manufacturing's ability to have sections of non-uniform thickness would allow for members of the FMS with less structural importance to consume less total mass to fulfill [UR-FMS-006]. Since these members could also be aligned to be parallel to light rays, it would also benefit [UR-FMS-020]. [UR-FMS-012] suggests an avoidance of support structures, a consideration that was of lesser priority to the group compared to other requirements. A future design should see the minimization of support structures by limiting the number of 90-degree overhangs.

The physical model used for testing correlation was printed out of ABS plastic using a Stratasys F270 3D printer available in the Rettner shop. While this physical model allows for testing and correlation to the predicted simulations, it isn't fully accurate to a final build performed by L3Harris, as the final version will be printed via DMLS with Invar. With an increased budget, an invar prototype could be possible, allowing for a more relevant correlation.

ACKNOWLEDGMENTS

The ME205 L3Harris Senior Design Team would like to first thank our sponsor, L3Harris, and the team members Patrick Ellsworth, Steve Sutton, Devin Woodyard, and Pat Zinter for their technical expertise and support. The authors would also like to acknowledge and thank Professor Muir, along with Jim Alkins, Chris Pratt, Ed Herger and Angel Bermudez for their mentorship and guidance throughout this semester. Finally, the authors would like to thank our peers in senior design, who have now been our classmates for the past four years in Mechanical Engineering at the University of Rochester. This project would not have been made possible without their willingness to share ideas, constructive feedback and insight.

REFERENCES

[1] Mohan, D. G., A, S., S, G., Jatti, V. S., S, K., and R, M. K., 2026, "Additive Manufacturing for Space Applications: A review of materials, methods, and future frontiers," China Welding, 35(1), p. 100010.

[2] Budynas, R. G., and Nisbett, J. K., 2015, *Shigley's Mechanical Engineering Design*, 10th ed., McGraw-Hill Education, New York, NY.

[3] Kanca, Y., 2023, "Effects of Normal Load and Sliding Distance on the Dry Sliding Wear Characteristics of Invar-36 Superalloy," *Erzincan University Journal of Science and Technology*, Vol. 16, No. 1, pp. 258–272. https://doi.org/10.18185/erzifbed.1250712.

[4] 3Dnatives, 2024, "The Complete Guide to Laser Powder Bed Fusion in 3D Printing," *3Dnatives*, accessed Apr. 26, 2026, https://www.3dnatives.com/en/direct-metal-laser-sintering100420174-2/.

[5] AIP Precision Machining, 2025, "Additive Manufacturing Aerospace Parts: When to Use It," *AIP Precision Machining*, accessed Apr. 26, 2026, https://aipprecision.com/aerospace-parts-manufacturing-when-to-choose-additive-over-traditional-machining/.

[6] Stephenson, T., Tricker, D., Tarrant, A., Michel, R., and Clune, J., 2015, "Physical and Mechanical Properties of LoVAR: A New Lightweight Particle-Reinforced Fe-36Ni Alloy," NASA Technical Reports Server, Report No. GSFC-E-DAA-TN24011, Goddard Space Flight Center, Greenbelt, MD.

[7] Wei, K., Yang, Q., Ling, B., Yang, X., Xie, H., Qu, Z., and Fang, D., 2020, "Mechanical Properties of Invar 36 Alloy Additively Manufactured by Selective Laser Melting," *Materials Science and Engineering: A*, Vol. 772, p. 138840.

[8] Renishaw plc, "Design for Metal AM: A Beginner's Guide," *Renishaw Resource Centre*, accessed Apr. 26, 2026, https://www.renishaw.com/resourcecentre/download/feature-article-design-for-metal-am-a-beginners-guide–111752.

[9] Tan, A. B. P., et al., 2020, "On Residual Stress Development, Prevention, and Compensation in Metal Additive Manufacturing," *Materials*, Vol. 13, No. 2, p. 255.

[10] Stratasys Ltd., 2026, "F270 3D Printer," *Stratasys Support Center*, accessed Apr. 26, 2026, https://support.stratasys.com/en/Printers/FDM-Legacy/F270.

[11] Stratasys Ltd., 2021, "F123 3D Printer Series Spec Sheet," Product Specification Sheet PSS_FDM_F123Series_0721a, Stratasys Ltd., Eden Prairie, MN.

[12] Online materials information resource - matweb [Online]. Available: https://www.matweb.com/.

[13] Siemens Digital Industries Software, *NX*.

[14] MathWorks Inc, 2025, *MATLAB*, Version R2025a

[15] Why do some alloys not expand when heated? | technology networks [Online]. Available: https://www.technologynetworks.com/applied-sciences/news/why-do-some-alloys-not-expand-when-heated-376935.

[16] BAE Systems Information and Electronic Systems Integration Inc., 2020, "Athermal Cassegrain Telescope," U.S. Patent No. 10,534,165, issued Jan. 14, 2020.

[17] Raytheon, “High-Stiffness Structure for Larger Aperture Telescope and Ground-Based Larger Aperture Telescope Using the Same,” European Patent No. EP 3 356 873 B1.

[18] L3Harris Technologies, Inc., “James Webb Space Telescope | L3Harris® Fast. Forward.,” accessed Apr. 25, 2026.

[19] Northrop Grumman Corp., “CERAFORM Silicon Carbide,” technical datasheet, accessed Apr. 25, 2026.

[20] Harnisch, B., et al., “Ultra-Lightweight C/SiC Mirrors and Structures,” *ESA Bulletin*, No. 95, 1998.

[21] Sein, E., Toulemont, Y., Safa, F., Duran, M., Deny, P., De Chambure, D., Passvogel, T., and Pilbratt, G., 2003, “A Φ 3.5 M SiC Telescope for HERSCHEL Mission.

[22] Mersen Boostec and Airbus Defence & Space, 2016, “The SiC Primary Mirror of the EUCLID Telescope,” *Proc. ICSO 2016*.

[23] NOAA NESDIS, 2026, “5 Ways NOAA’s Satellites Support Emergency Managers and First Responders,” accessed Apr. 25, 2026.

[24] NOAA NESDIS, 2024, “Tackling Global Food Security With the Help of LEO Satellite Vegetation Health Products,” accessed Apr. 25, 2026.

[25] NASA, 2025, “NASA-ISRO Mission Will Map Farmland From Planting to Harvest,” accessed Apr. 25, 2026.

[26] NASDA, 2025, “NASA Satellite Technology Advances NASS Agricultural Data Collection,” accessed Apr. 25, 2026.

[27] NIST, 2025, “An Evaluation of Dependencies of Critical Infrastructure Timing Services on the Global Positioning System (GPS),” NIST Technical Note 2189.

[28] NIST, “Process-Structure-Properties Investigations for Laser Powder Bed Fused IN718 Built on IN625 Substrate,” data publication, accessed Apr. 25, 2026.

[29] ASME, 2020, “Advancing Additive Manufacturing in Aerospace,” accessed Apr. 25, 2026.

[30] Manufacturing Technology Centre, 2022, “Environmental Impact of Metal Additive Manufacturing,” accessed Apr. 25, 2026.

[31] Gonçalves, A., Ferreira, B., Leite, M., and Ribeiro, I., 2023, “Environmental and Economic Sustainability Impacts of Metal Additive Manufacturing: A Study in the Industrial Machinery and Aeronautical Sectors,” *Sustainable Production and Consumption*, 42, pp. 292–308.

[32] Khalid, M., and Peng, Q., 2021, “Sustainability and Environmental Impact of Additive Manufacturing: A Literature Review,” *Computer-Aided Design and Applications*, 18(6), pp. 1210–1232.

[33] Farinia Group, 2015, “Environmental Impact of Metal Additive Manufacturing,” accessed Apr. 25, 2026.

[34] The International Nickel Company, inc, 2011, “36% Nickel-Iron Alloy For Low Temperature Service”.

[35] Edmund Optics, “Understanding Optical Specifications”.

[36] “Suggested Tightening Torque1 Values to Produce Corresponding Bolt Clamping Loads,” Sabre Industrial Supplies LTD.

ANNEX A

ADMINISTRATIVE FIGURES

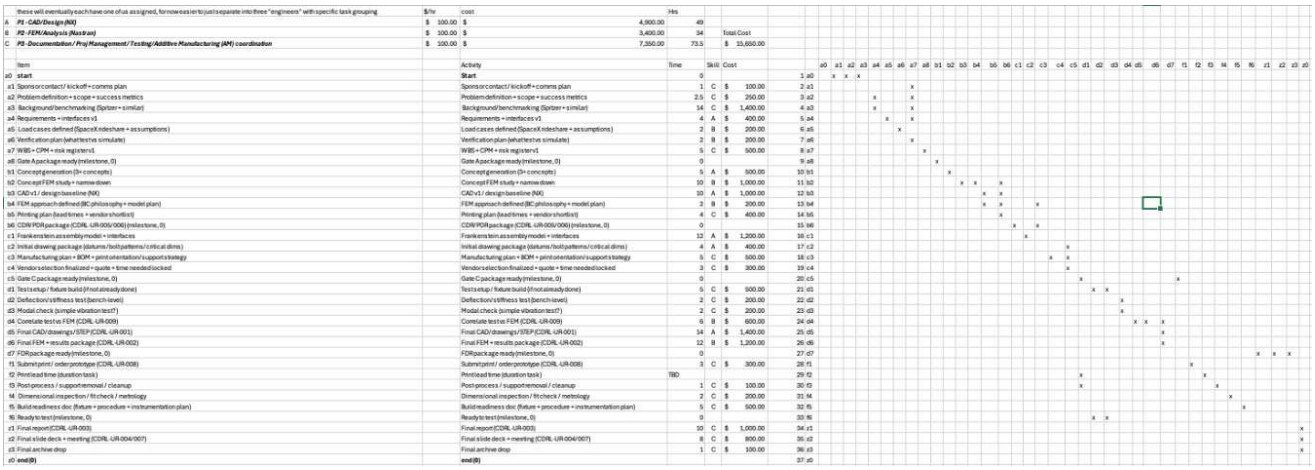

Figure 1: Excel Spreadsheet for Critical Path Method MATLAB Code.

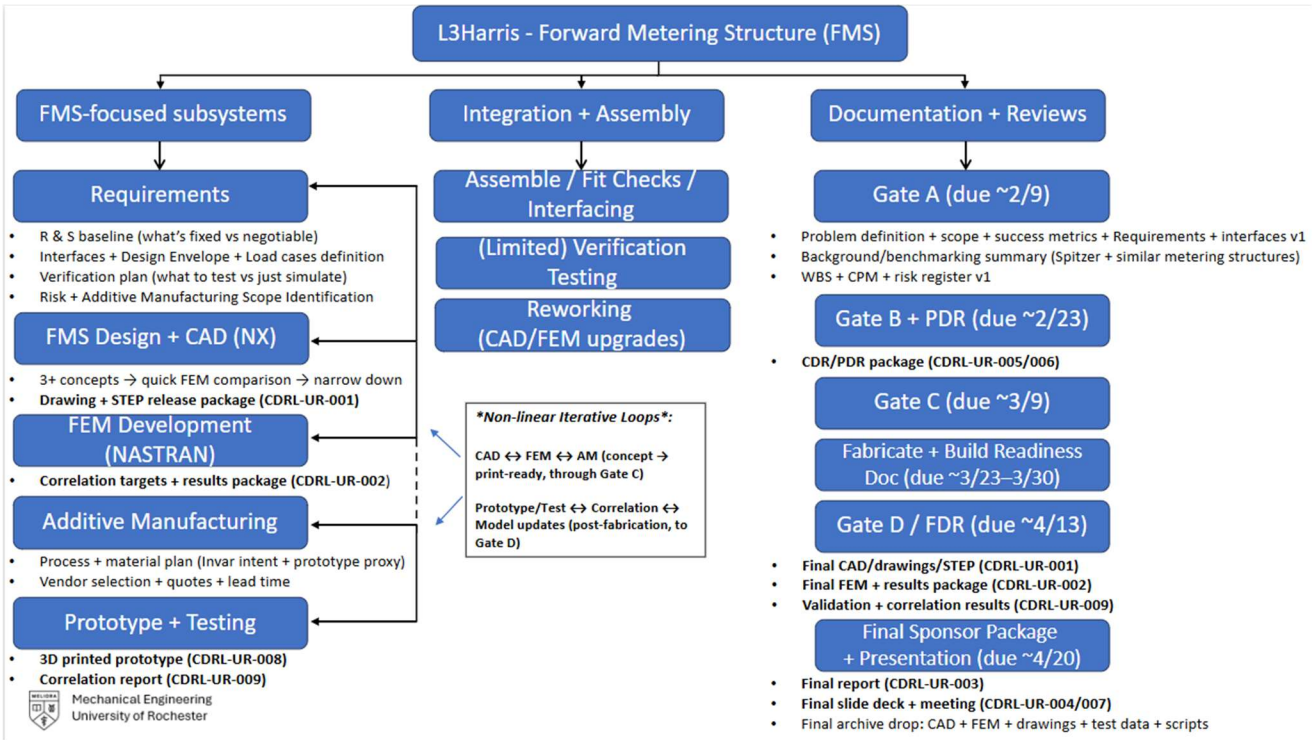

Figure 2: Work Breakdown Structure (WBS).

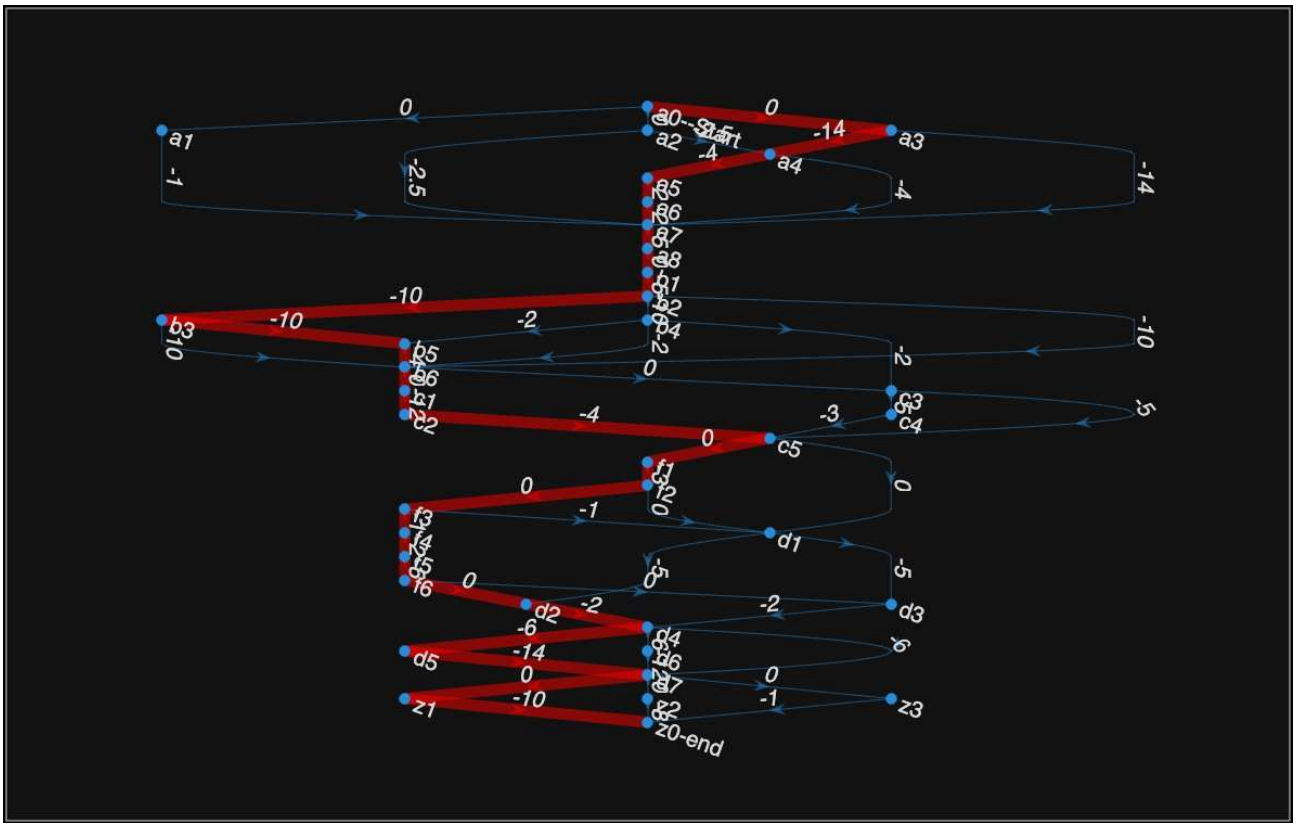

Figure 3: Critical Project Path of Work Breakdown Tasks Visualization Generated in MATLAB.

ANNEX B

PRELIMINARY DESIGN CONCEPT ANALYSIS

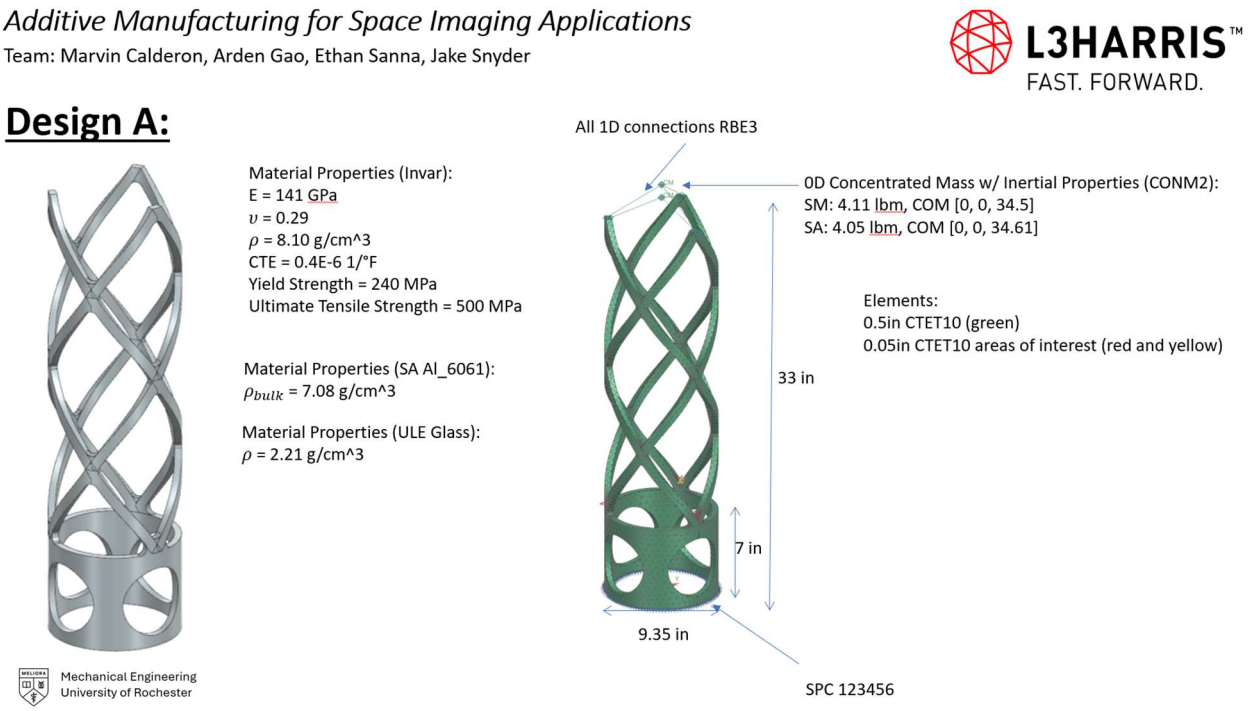

Figure 1: Design A FEM setup details.

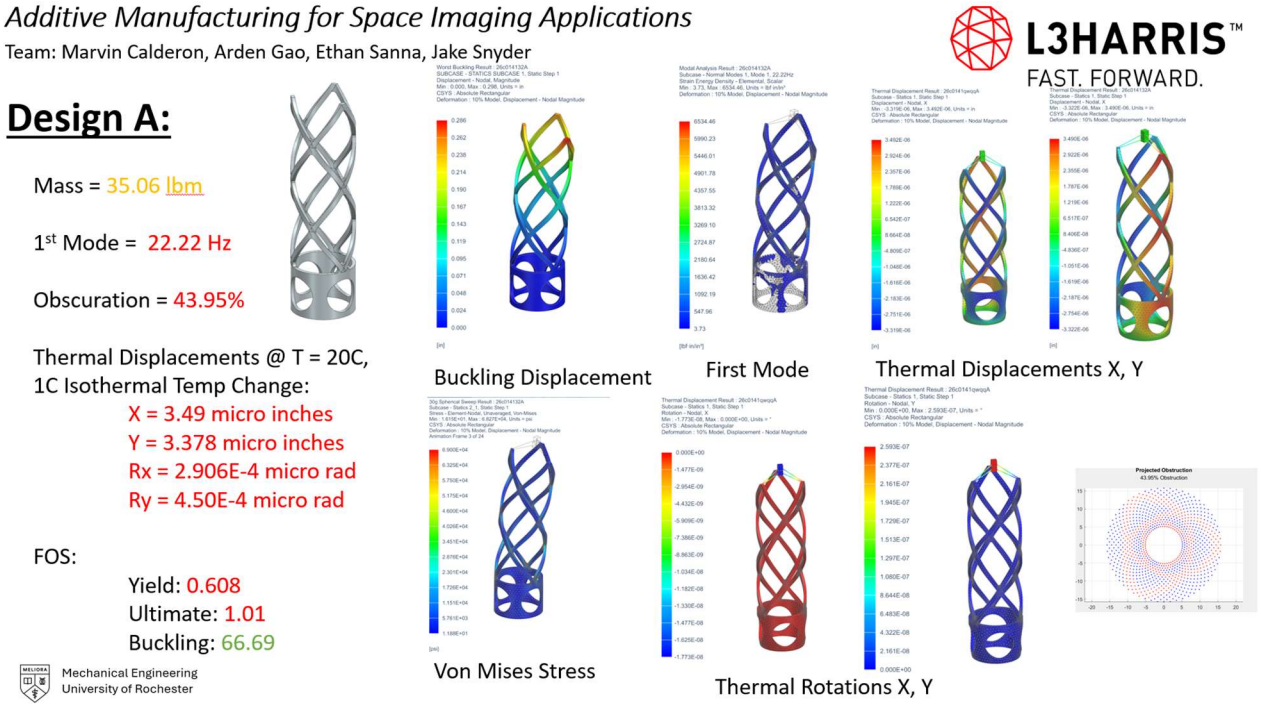

Figure 2: Design A analysis results.

Additive Manufacturing for Space Imaging Applications

Team: Marvin Calderon, Arden Gao, Ethan Sanna, Jake Snyder

L3HARRIS™ FAST. FORWARD.

Design B:

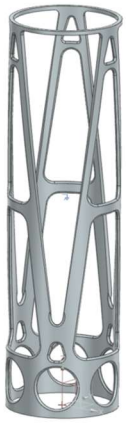

Material Properties (Invar):
E = 141 GPa
υ = 0.29
ρ = 8.10 g/cm^3
CTE = 0.4E-6 1/°F
Yield Strength = 240 MPa
Ultimate Tensile Strength = 500 MPa

Material Properties (SA Al_6061):
ρ_{bulk} = 7.08 g/cm^3

```
% Calculate SA bulk density
SA_volume = 259.40722; % cm^3, 15.83 in^3
instrument_mass = 1133.98; % g, 2.5 lbm
Al_density = 2.711; % g/cm^3
density = Al_density + instrument_mass/SA_volume % g/cm^3
```

Material Properties (ULE Glass):
ρ = 2.21 g/cm^3

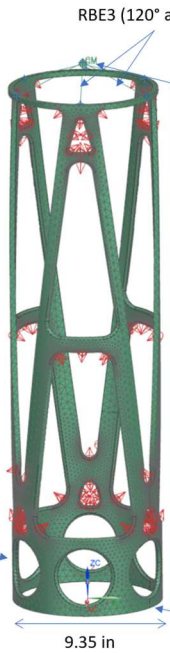

0D Concentrated Mass w/ Inertial Properties (CONM2):
SM: 4.11 lbm, COM [0, 0, 34.5]
SA: 4.05 lbm, COM [0, 0, 34.61]

Elements:
0.5in CTET10 (green)
0.1in CTET10 areas of interest (red)

Mechanical Engineering
University of Rochester

Figure 3: Design B FEM setup details.

Additive Manufacturing for Space Imaging Applications

Team: Marvin Calderon, Arden Gao, Ethan Sanna, Jake Snyder

L3HARRIS™ FAST. FORWARD.

Design B:

Mass = 25.47 lbm

1st Mode = 61.04 Hz

Obscuration = 33.73%

Thermal Displacements @ T = 20C,
1C Isothermal Temp Change:
X = 4.15E-4 micro inches
Y = 7.45E-4 micro inches
Rx = 9.94E-5 micro rad
Ry = 4.03E-5 micro rad

FOS:
Yield: 2.31
Ultimate: 4.39
Buckling: 11.81

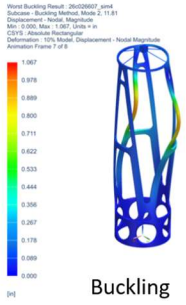

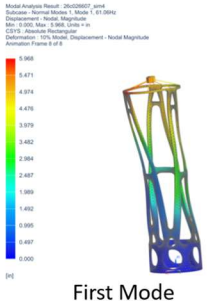

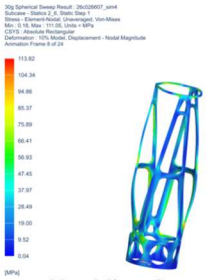

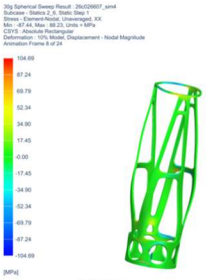

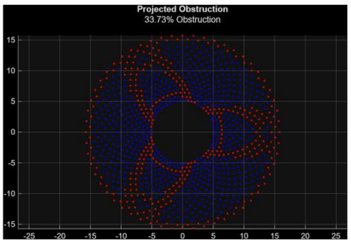

Mechanical Engineering
University of Rochester

Figure 4: Design B structural analysis results.

Additive Manufacturing for Space Imaging Applications

Team: Marvin Calderon, Arden Gao, Ethan Sanna, Jake Snyder

L3HARRIS™ FAST. FORWARD.

Design B:

Mass = 25.47 lbm

1st Mode = 61.04 Hz

Obscuration = 33.73%

Thermal Displacements @ T = 20C, 1C Isothermal Temp Change:

X = 4.15E-4 micro inches
Y = 7.45E-4 micro inches
Rx = 9.94E-5 micro rad
Ry = 4.03E-5 micro rad

FOS:

Yield: 2.31
Ultimate: 4.39
Buckling: 11.81

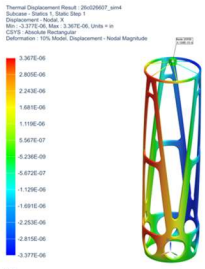

Thermal Displacement X

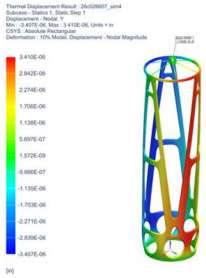

Thermal Displacement Y

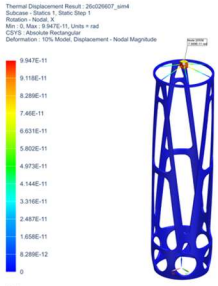

Thermal Rotation X

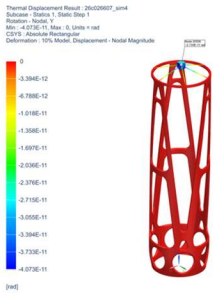

Thermal Rotation Y

Mechanical Engineering
University of Rochester

Figure 5: Design B thermal analysis results.

Additive Manufacturing for Space Imaging Applications

Team: Marvin Calderon, Arden Gao, Ethan Sanna, Jake Snyder

L3HARRIS™ FAST. FORWARD.

Design C:

Material Properties (Invar):
E = 141 GPa
υ = 0.29
ρ = 8.10 g/cm^3
CTE = 0.4E-6 1/°F
Yield Strength = 240 MPa
Ultimate Tensile Strength = 500 MPa

Material Properties (SA Al_6061):
ρ_{bulk} = 7.08 g/cm^3

```
% Calculate SA bulk density
SA_volume = 259.40722; % cm^3, 15.83 in^3
instrument_mass = 1133.98; % g, 2.5 lbm
Al_density = 2.711; % g/cm^3
density = Al_density + instrument_mass/SA_volume % g/cm^3
```

Material Properties (ULE Glass):
ρ = 2.21 g/cm^3

t=0.425 in
(Thickness taken from average feature thickness of midsurface object)

RBE3 (120° apart)

0D Concentrated Mass w/ Inertial Properties (CONM2):
SM+SA: ~15 lbm

Elements:
2D Mesh (Midsurface Shell of FMS)

Quad4 (Element Size = 0.157")

33 in

5 in

9.35 in

SPC 123456

Mechanical Engineering
University of Rochester

Figure 6: Design C FEM setup details.

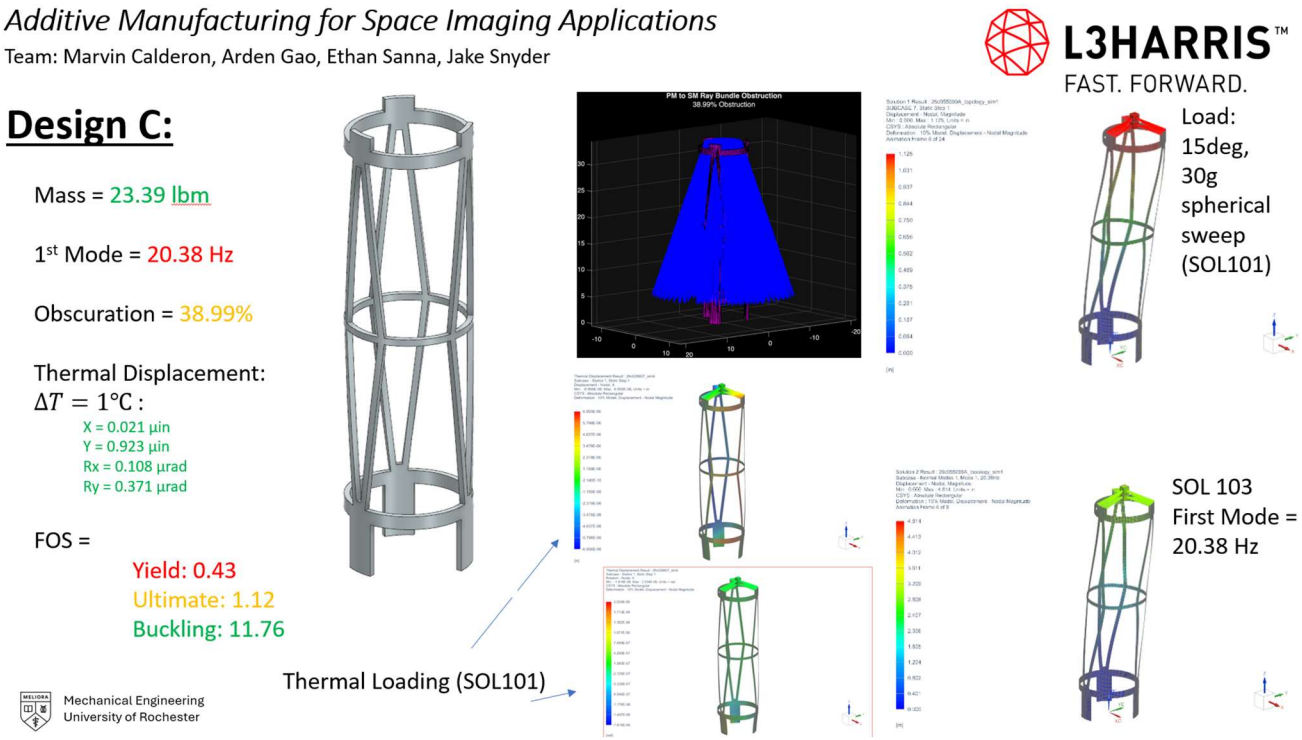

Figure 7: Design C analysis results.

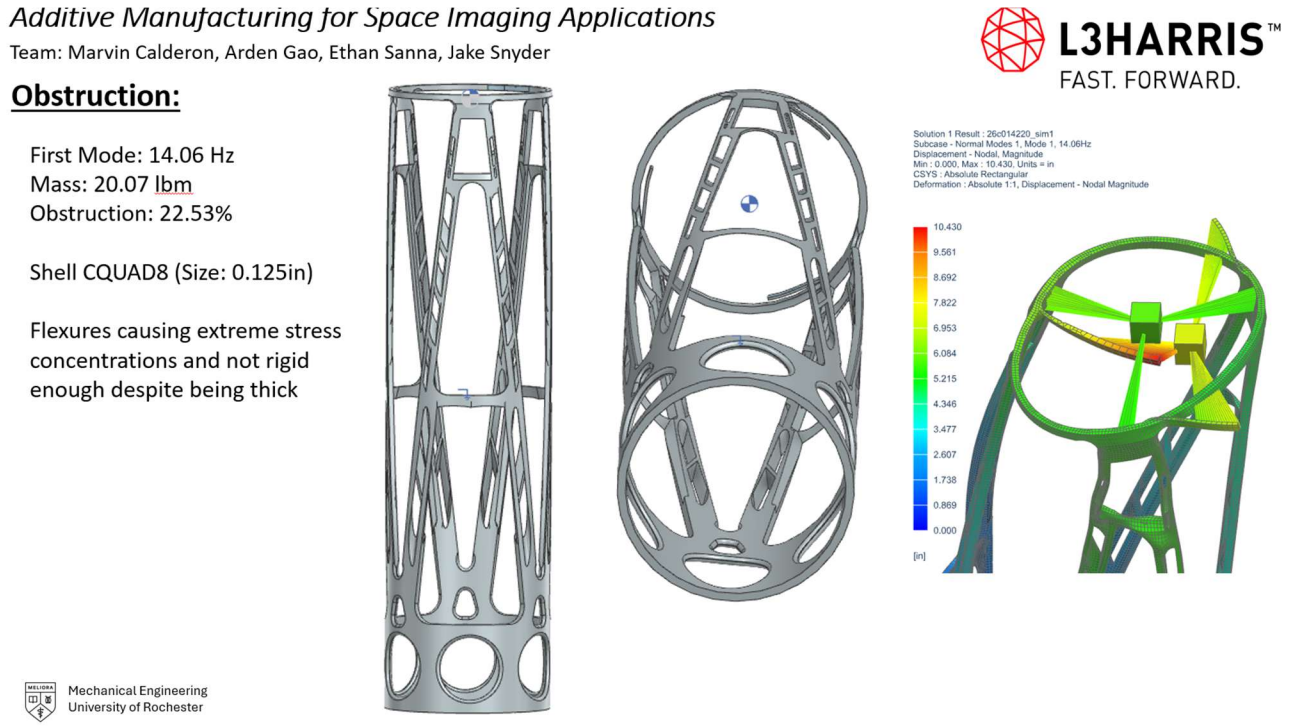

Figure 8: Design D analysis.

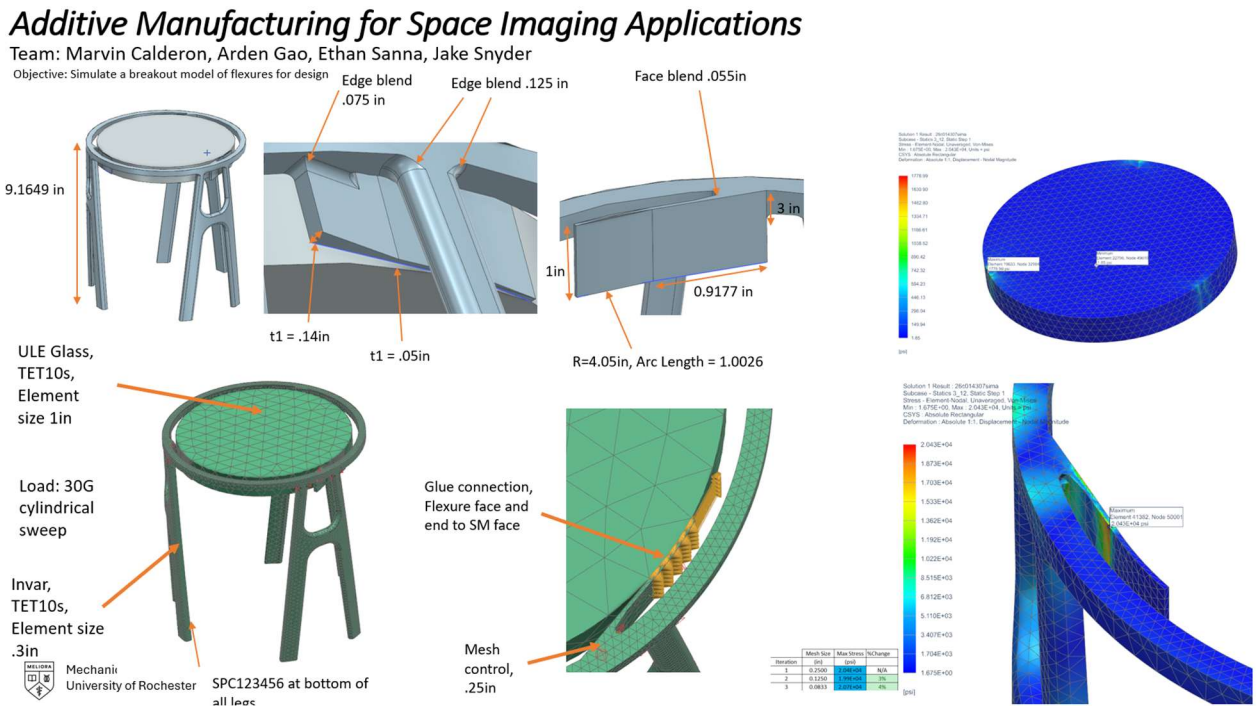

Figure 9: Design E design analysis.

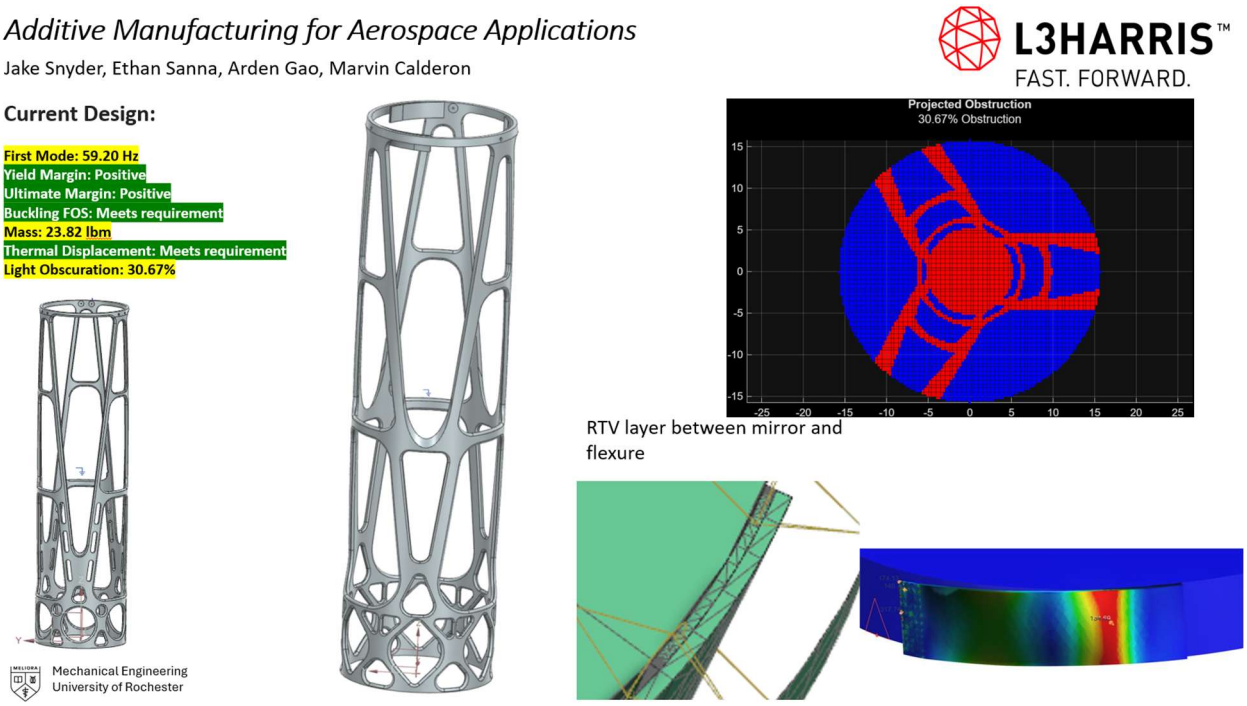

Figure 10: Design F design analysis.

ANNEX C

FINAL DESIGN ANALYSIS

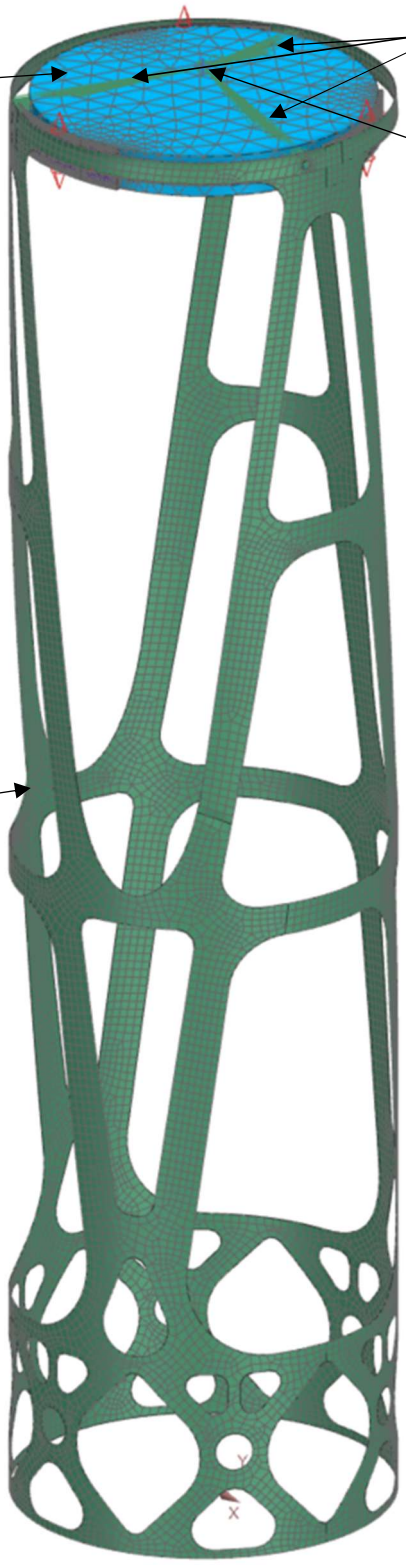

Figure 1: FEM setup overview.

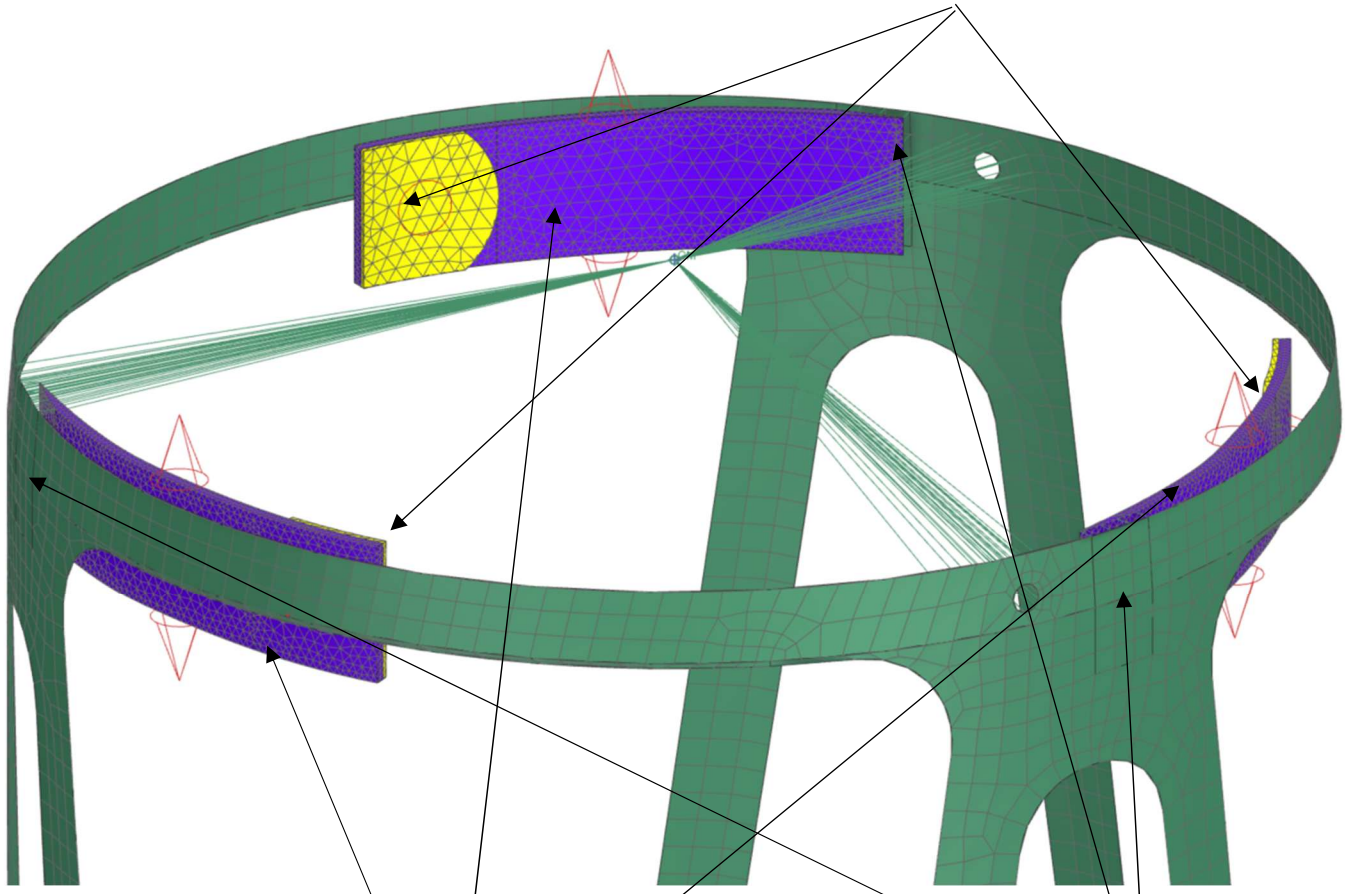

Figure 2: Detailed breakdown of FEM for the top of the FMS and relevant interfaces.

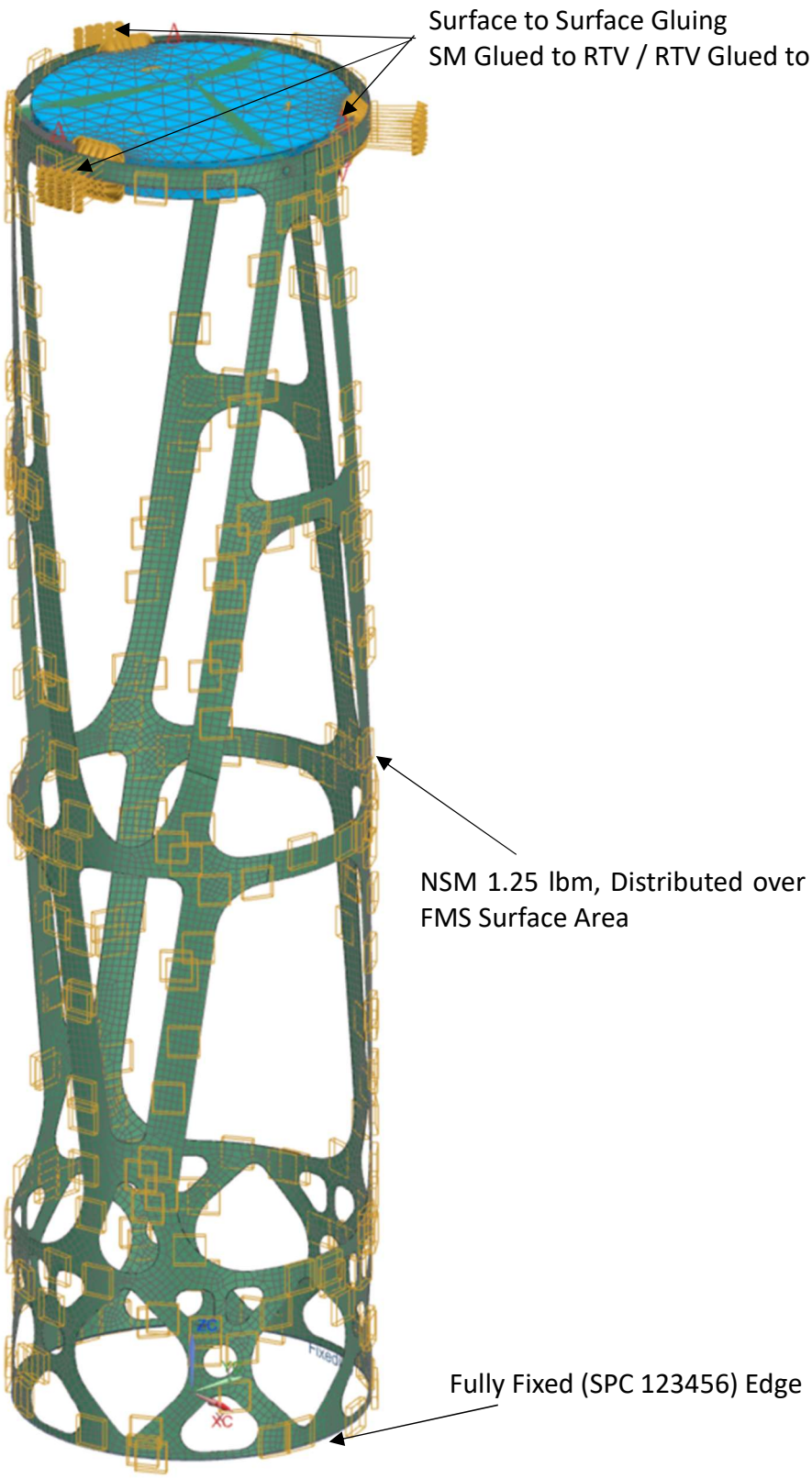

Figure 3: SIM setup with specified nonstructural mass and surface-to-surface gluing. See Mechanical Analysis Section 4: Computer Based Analysis for details about each solution per requirement.

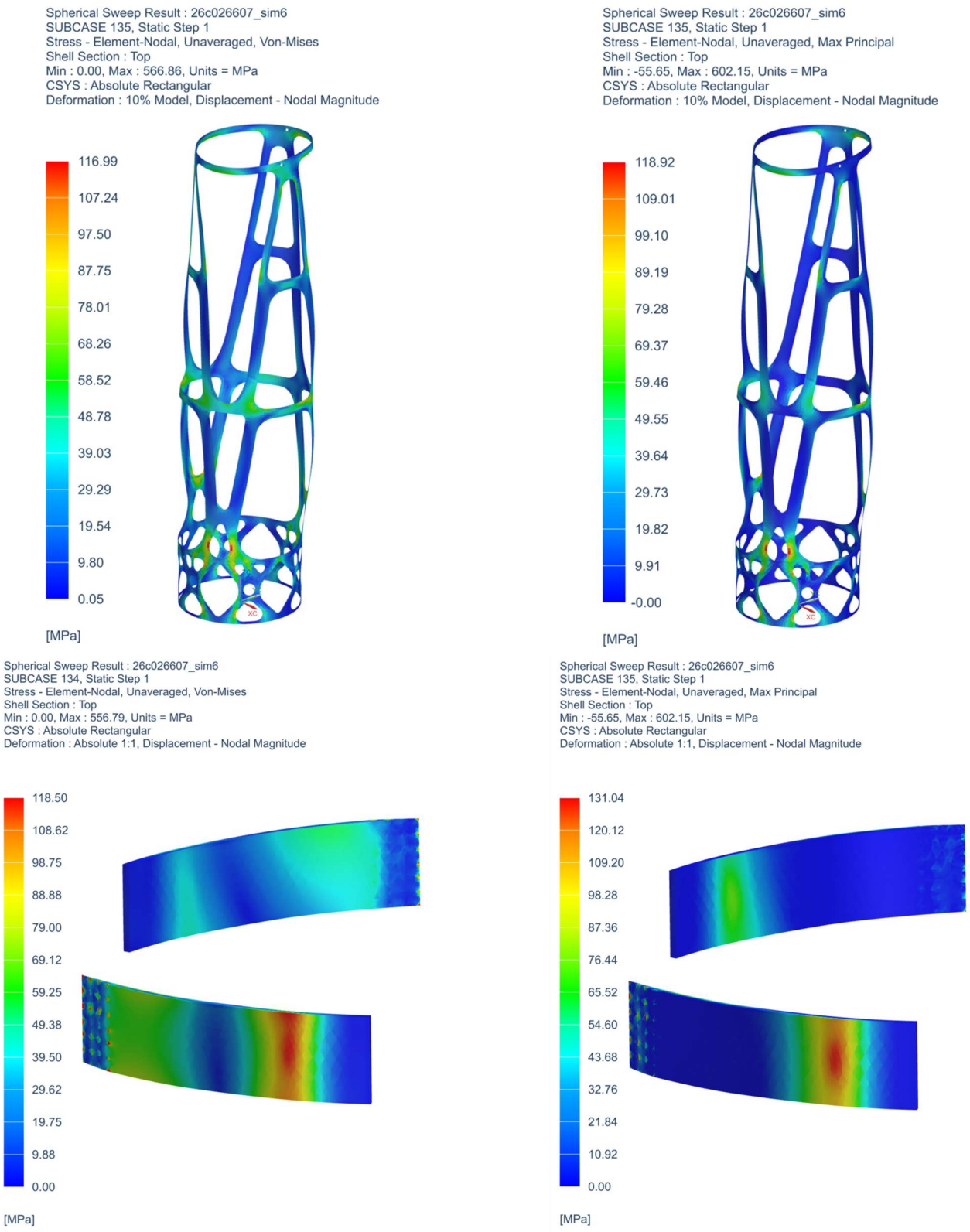

Figure 4: Results for Yield stress (left) and Ultimate stress (right) for FMS.

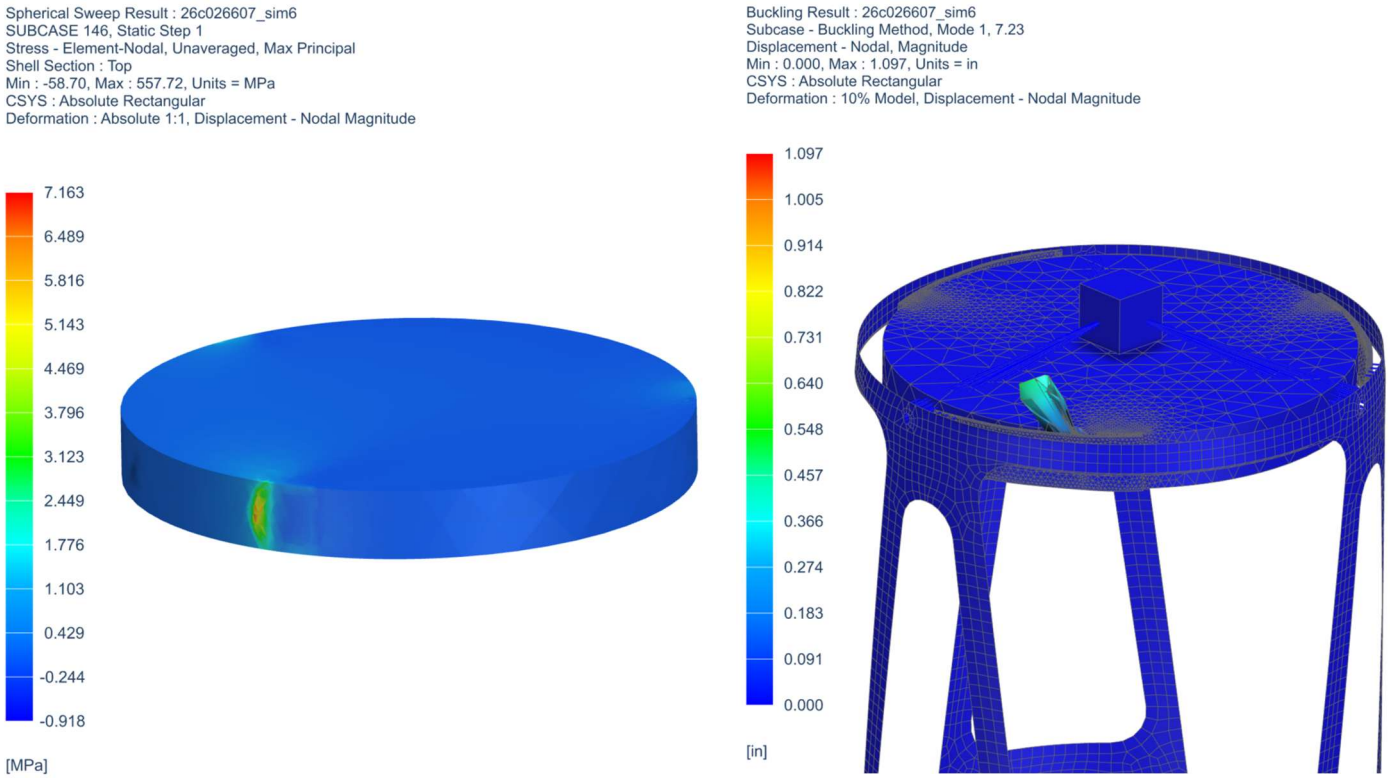

Figure 5: Ultimate stress for SM and lowest positive eigenvalue buckling. The RTV is the limiting component for buckling analysis as it fails first.

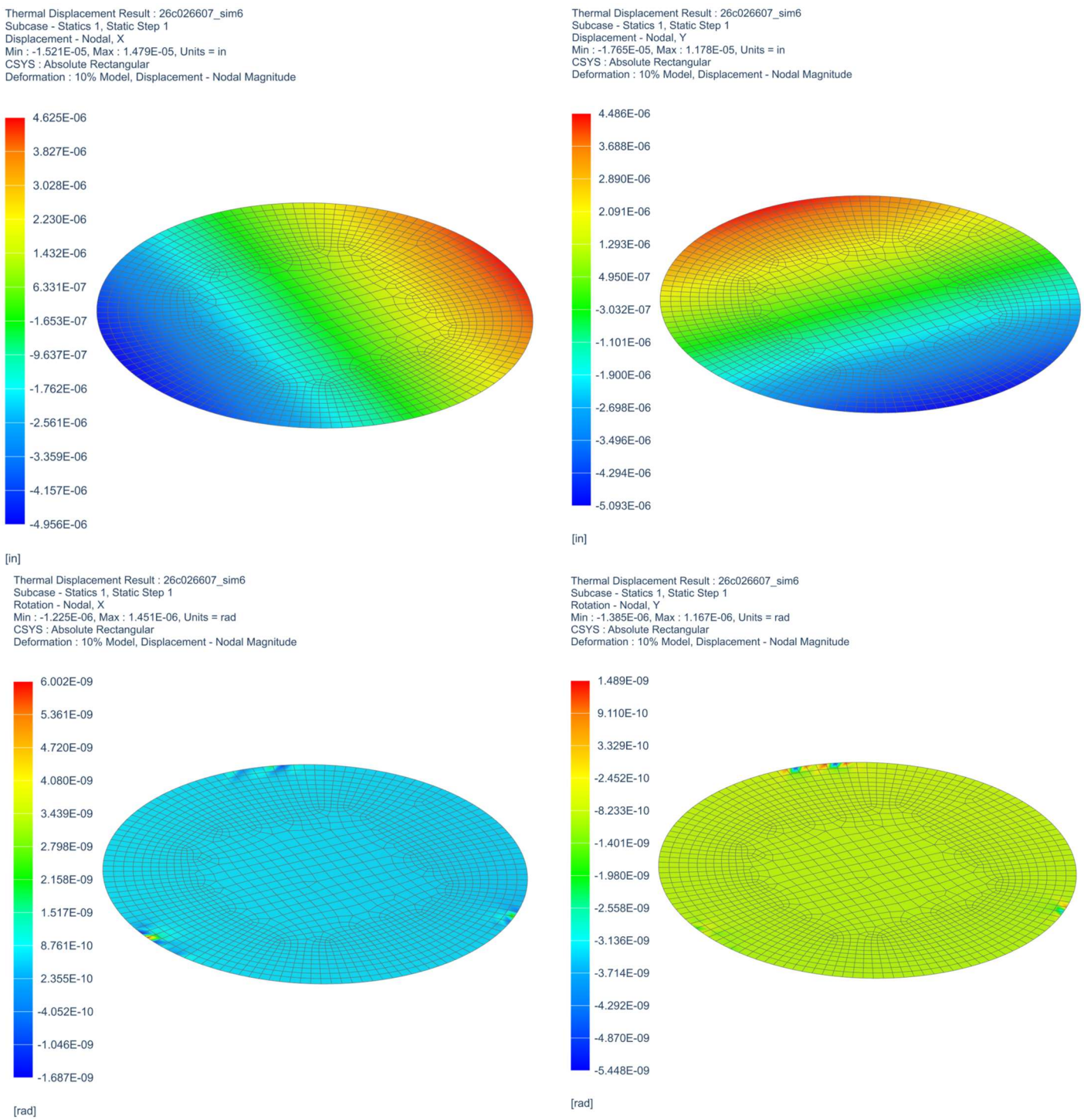

Figure 6: Thermal displacements in accordance to [UR-FMS-003].

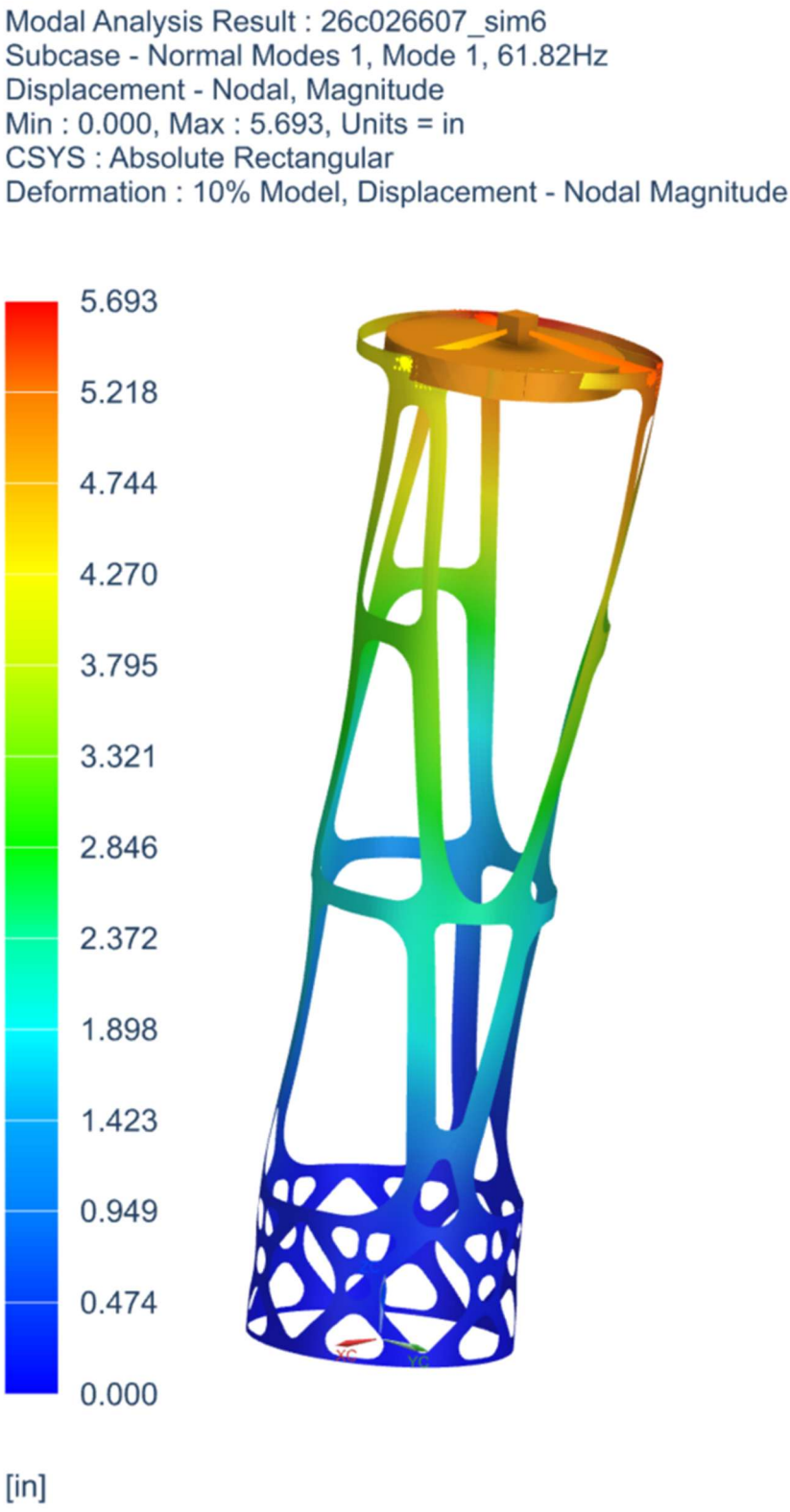

Figure 7: First mode in compliance with [UR-FMS-007]. The mode shape rocks back and forth.

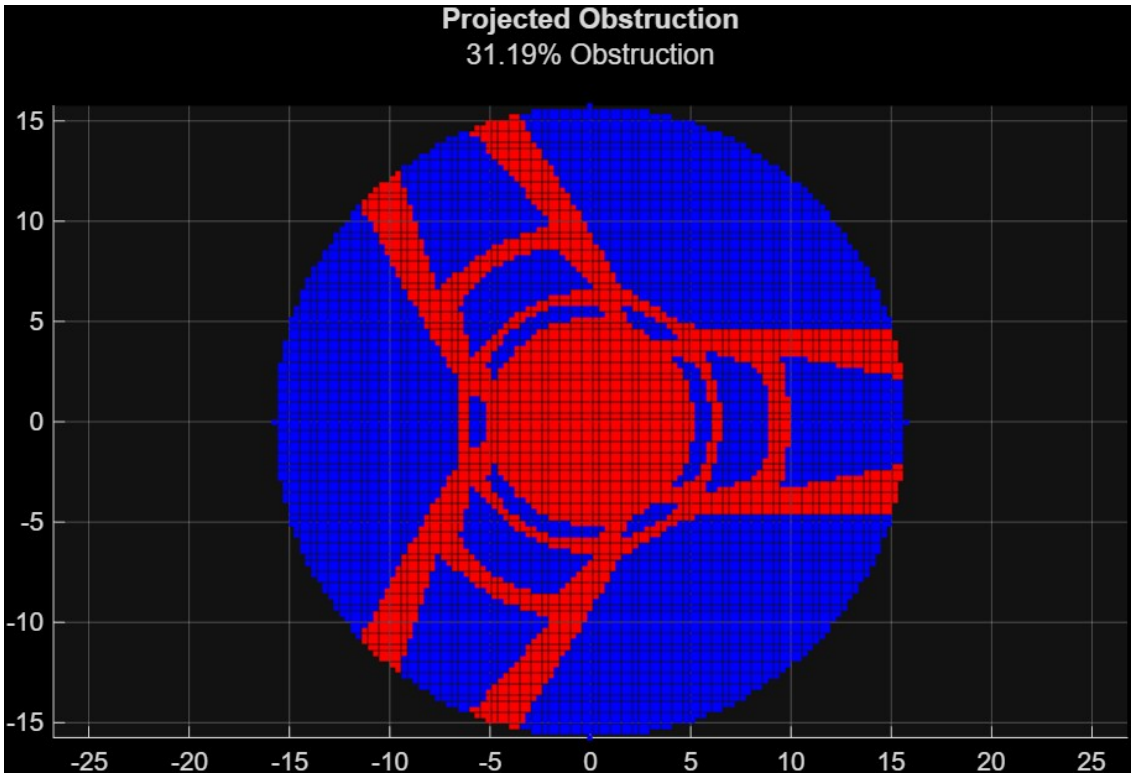

Figure 8: MATLAB script output to evaluate obstruction as a 2D projection onto the PM. High definition ray package consisted of 9845 unique rays that were checked for intersection with the FMS [UR-FMS-020].

Additive Manufacturing for Space Imaging Applications

Team: Marvin Calderon, Arden Gao, Ethan Sanna, Jake Snyder

L3HARRIS™ FAST. FORWARD.

Tolerance Analysis:

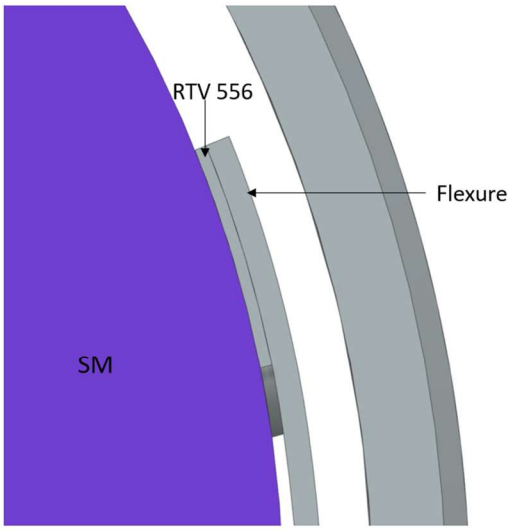

Edmund Optics Mirror Tolerance (SM): +0/-0.00039in

Seido Systems L-PBF Tolerance (Flexure): +/- 0.00240in

Stack Up Case 1: -0.00039 in - 0.00240 in = -0.00201 in

Stack Up Case 2: 0 in + 0.00240 in = 0.00240 in

RTV 556 Nominal Thickness: 0.040 in

Tolerance: $0.040\ ^{+0.00240}_{-0.00201}$ in

Mechanical Engineering
University of Rochester

Figure 9: Worst case stack up tolerance analysis. Tolerances courtesy of Edmund Optics and Seido Systems.

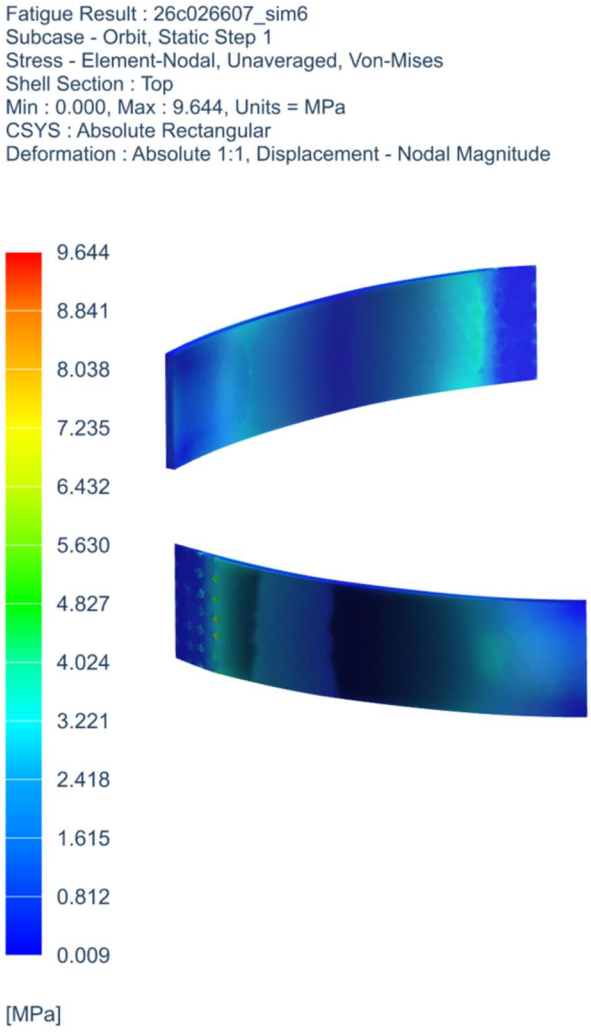

Figure 10: Fatigue analysis reveals an infinite life in orbit under 21°C±1°C.

Bolt Pretension and Torque:

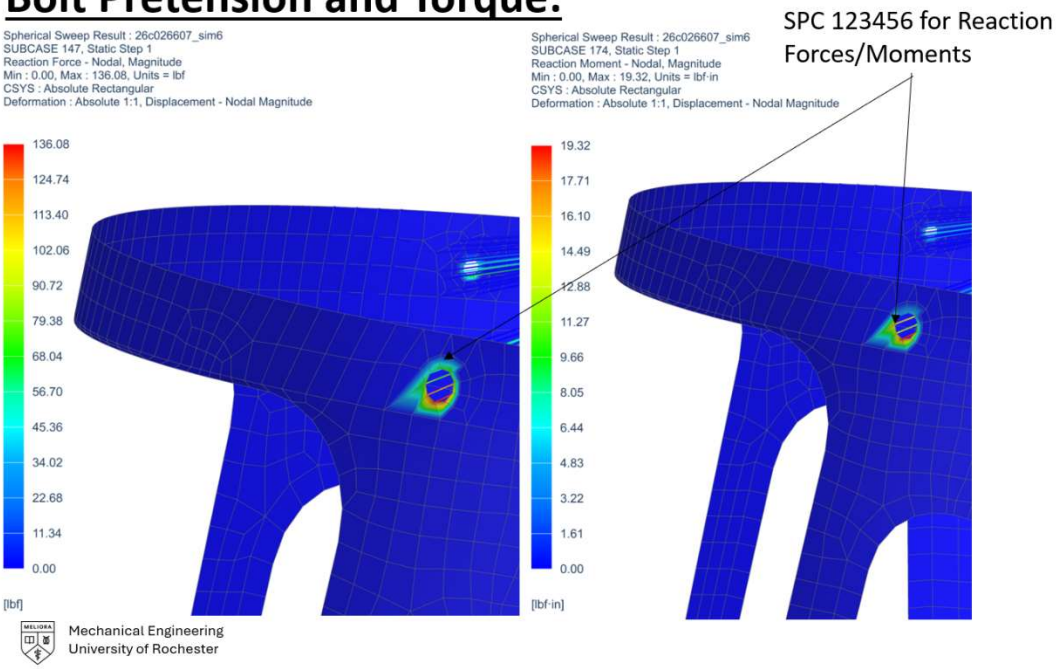

SAE Grade 2 #6-32 Bolt:

$$F_{PL} = \%_{yield} S_{ty} A_t$$
$$= 77\% * 74{,}000 * 0.00909$$
$$= 517.948\ lbf$$

$$T = K_T d_{nom} F_{PL}$$
$$= 0.2 * 0.138 * 517.948$$
$$= 14.295\ lbf \cdot in$$

Figure 11: SPC 123456 added to each bolt hole to approximate reaction forces. Bolt preload and required torque are both within standard #6-32 bolt strengths and maximum tensile load experienced.

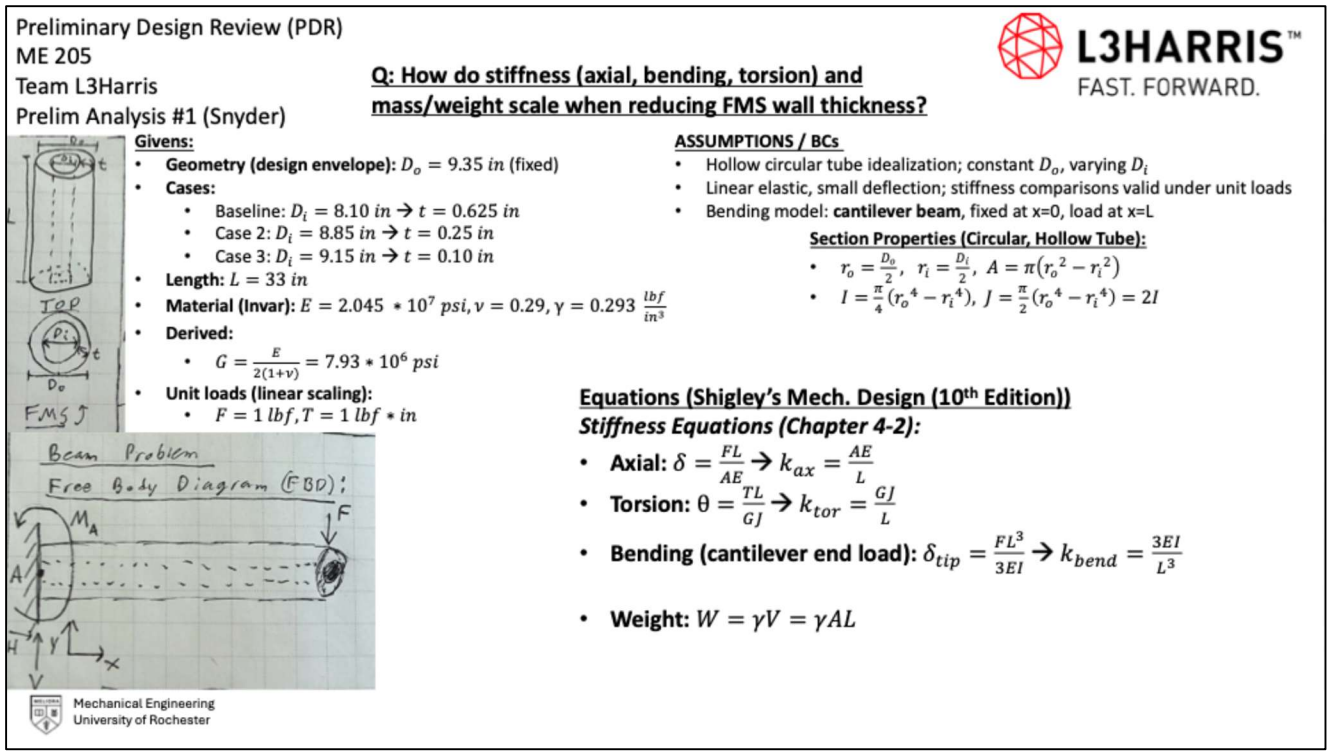

Figure 12: Hand-calculation setup (geometry + FBDs) for an envelope-constrained hollow-tube baseline used to compare stiffness and weight scaling.

Preliminary Design Review (PDR)
ME 205
Team L3Harris
Prelim Analysis #1 (Snyder)

L3HARRIS™ FAST. FORWARD.

Results

Case	t (in)	A (in²)	I (in⁴)	J (in⁴)	W (lbf)	k_{ax}(lbf/in)	k_{bend}(lbf/in)	k_{tor}(lbf·in/rad)
Baseline	0.625	17.13	163.85	327.7	165.63	1.06E7	2.80E5	7.87E7
t = 0.25"	0.25	7.15	74.04	148.08	69.13	4.43E6	1.26E5	3.56E7
t = 0.10"	0.10	2.91	31.08	62.16	28.14	1.80E6	5.30E4	1.49E7

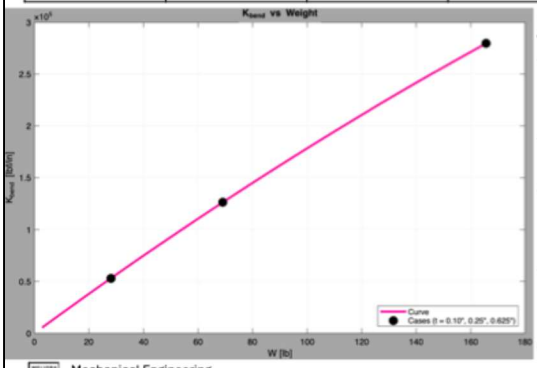

Mechanical Engineering
University of Rochester

Design Impact:

- ***With E,G, and L fixed:***
  - $k_{ax} \propto A, k_{bend} \propto I, k_{tor} \propto J$
- Thin-wall reduction from t = 0.625" to 0.10" cuts weight to ~17% of baseline, but cuts bending/torsional stiffness to 19%.
- In the thin-wall range (0.25→0.10 in), stiffness becomes sensitive: per 0.01 in thickness reduction, k_{bend} drops by about 4.87*10^3 lbf/in and weight drops by about 2.73 lbf.
- This tube baseline establishes a reference stiffness-to-weight curve that future concepts (tripod/ring-tower/lattice) should exceed.
- **Design decision**: concepts should preserve stiffness efficiently (maintain large effective I,J using outer-radius load paths: rings/shell ribs/truss attachments) instead of relying on thick walls.

Figure 13: Results for stiffness and weight versus wall thickness (including bending stiffness-to-weight trade) for the hollow-tube baseline.

Preliminary Design Review (PDR)
ME 205
Team L3Harris
Prelim Analysis #2 (Snyder)

L3HARRIS™ FAST. FORWARD.

Q: Under a 1°C isothermal change, how tight must symmetry/thermal uniformity be at the 3 Secondary Mirror (SM) flexures to meet the UR-FMS-003 rotation and translation limits?

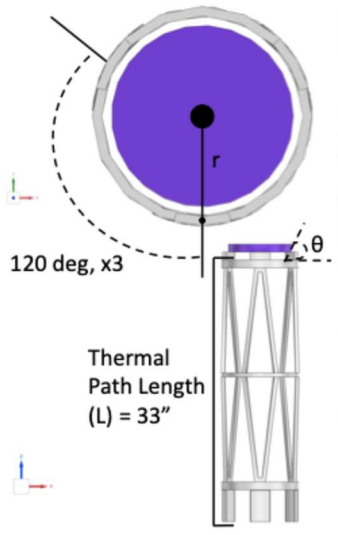

Mechanical Engineering
University of Rochester

Givens:

- **Requirement (UR-FMS-003):** under 1°C isothermal change:
  - translation (RSS X,Y) ≤ 7.87 µin
  - rotation (RSS Rx,Ry) ≤ 0.9 µrad
- **Example Flexure radius:** r = 4.05 in (SM dia 8.1 in)
- **Thermal path length:** L = 33 in
- **Invar CTE (α):** $0.72 * 10^{-6}/°C$

ASSUMPTIONS / BCs

- 3 identical flexure supports, 120° apart; small-angle approximation
- Linear thermal expansion; misalignment driven by differential temperature between supports
- Interface treated as rigid compared to flexure mismatch

Equations (Shigley's Mech. Design (10th Edition))

Shigley Temperature Effects:

- $\Delta L = \alpha L \Delta T$
- **Differential growth from support-to-support temperature mismatch:**
  - $\delta = \alpha L \Delta T_{diff}$
- **Small-angle tilt due to differential growth:**
  - $\theta = \frac{\delta}{r} \rightarrow \Delta T_{diff,allow} = \frac{\theta_{max} r}{\alpha L}$

Results ($\Delta T = 1$°C):

- **Common-mode growth:**
  $$\Delta L = \alpha L \Delta T = 23.8 \mu in$$
- **Rotation limit implies allowable differential growth:**
  $$\delta_{allow} = \theta_{max} r \approx 3.65 \mu in$$
- **Allowable temperature mismatch between supports:**
  $$\Delta T_{diff,allow} = \frac{\theta_{max} r}{\alpha L} \approx 0.15°C$$

Design Impact:

- To satisfy UR-FMS-003, the three SM flexure locations must be thermally matched to roughly ±0.15°C, this forces strict 3-fold symmetry in design geometry and thermal hardware placement (the flexures).

Figure 14: Hand calculations for isothermal temperature change specification to find thermally induced displacements and rotations.

ANNEX D

MATERIAL TESTING AND ANALYSIS CORRELATION

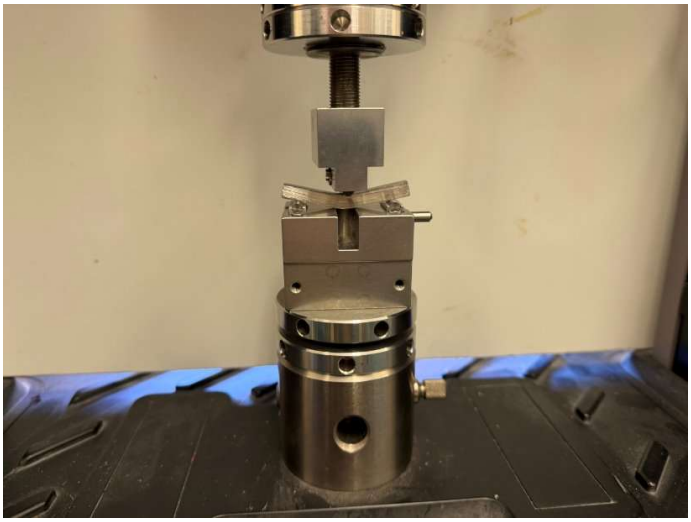

Figure 1: 3-Point-Bend test apparatus.

Figure 2: 3-Point-Bend results.

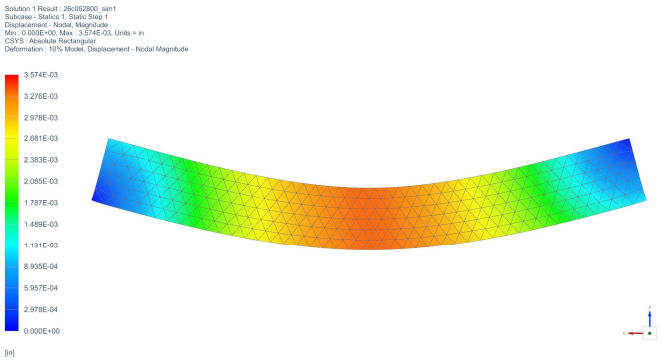

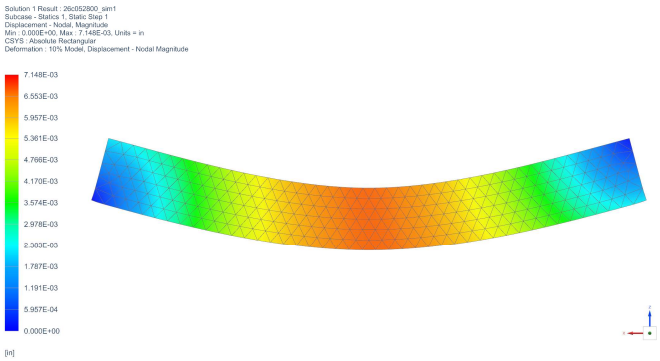

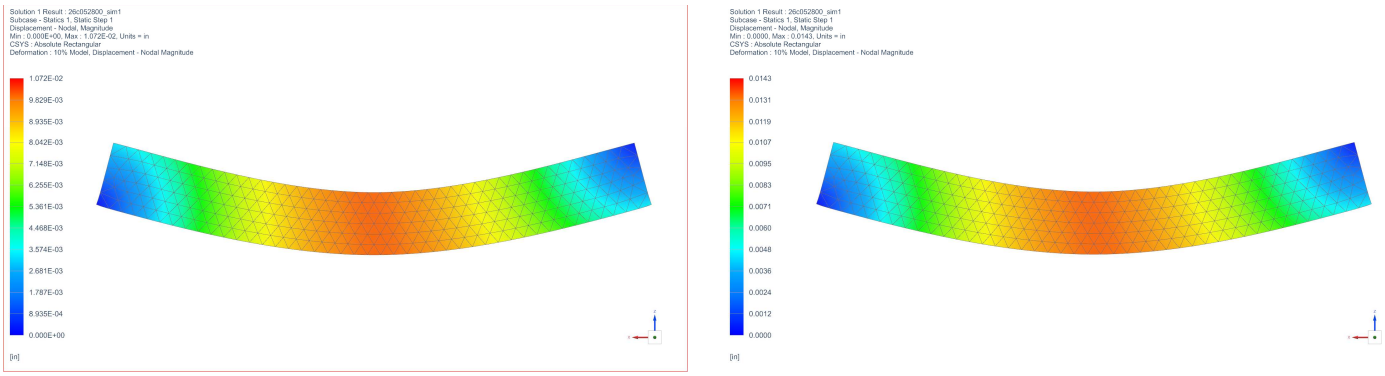

Figure 3: 3-Point-Bend NX test for (100 lbf, 200 lbf, 300 lbf, and 400 lbf).

Figure 4: CTE test apparatus.

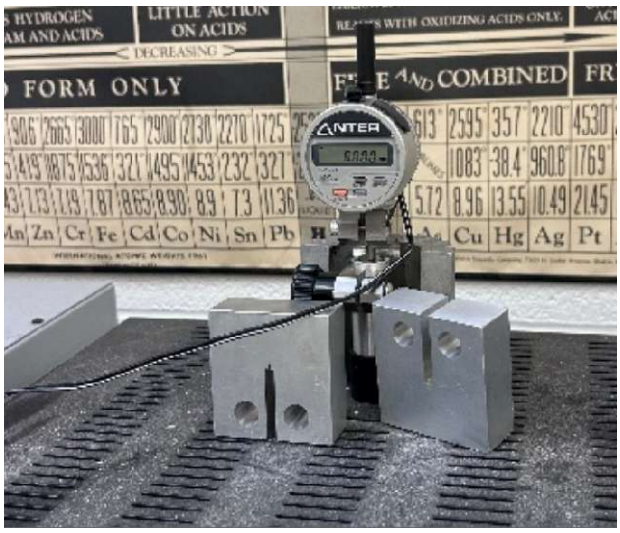

Figure 5: Displacement sensor (flawed).

Figure 6: Oxidized Invar.

```
clc;
clear;
close all;
% EXPERIMENTAL DATA
data = readtable('Invar 3pt bend 2026.txt');
load_experimental = data{:,1};
deflection_experimental = data{:,2};
time = data{:,3};
figure;
plot(deflection_experimental, load_experimental, 'LineWidth', 1.5, 'Color', 'r');
xlabel('Deflection (in)')
ylabel('Load (lbf)');
title('3-Point Bend Test with MTS Machine')
grid on;
% NX SIM DATA
load_NX = [0, 100, 200, 300, 400, 500, 600, 700, 800]; % lbf
deflection_NX = [0, 3.574E-03, 7.148E-03, 1.072E-02, 1.43E-02, 0.0179, 0.0214, 0.025,
0.0286]; % in
```

```
figure;
plot(deflection_NX, load_NX,'LineWidth', 1.5, 'Color', 'b')
xlabel('Deflection (in)')
ylabel('Load (lbf)');
title('3-Point Bend Test with Siemens NX')
grid on;
% EXPERIMENTAL VS NX
figure;
plot(deflection_experimental, load_experimental, 'r', 'LineWidth', 1.5);
hold on;
plot(deflection_NX, load_NX, 'bo--', 'LineWidth', 1.5, 'MarkerSize', 8);
xlabel('Deflection (in)');
ylabel('Load (lbf)');
title('Experimental Data vs Simulated Data');
legend('Experimental', 'NX Simulation', 'Location', 'best');
grid on;
% Given Values
L = 2.128; % in
b = 0.247; % in
h = 0.247; % in
% Stress and Strain
strain_exp = (6.*deflection_experimental.*h)./(L^2);
stress_exp = (3.*load_experimental.*L)./(2.*b.*h^2);
strain_NX = (6 .* deflection_NX .* h) ./ (L^2);
stress_NX = (3 .* load_NX .* L) ./ (2 .* b .* h^2);
% Comparison
figure;
plot(strain_exp, stress_exp, 'r', 'LineWidth', 1.5);
hold on;
plot(strain_NX, stress_NX, 'bo--', 'LineWidth', 1.5, 'MarkerSize', 8);
xlabel('Strain');
ylabel('Stress (psi)');
title('Stress vs Strain (3-Point Bending)');
legend('Experimental', 'NX Simulation', 'Location', 'best');
grid on;
```

Figure 7: MATLAB code for 3-point-bend.

```
clc;
clear;
close all;
% aluminum data
temperature_Al = [24 106 209 311]; % Celsius
displacement_Al = [0 5.758 9.713 13.222]; % mm
displacement_Al_inches = displacement_Al * 0.0393701;
% relative change
dT_Al = temperature_Al - temperature_Al(1);
dL_Al = displacement_Al_inches - displacement_Al_inches(1);
p_Al = polyfit(dT_Al,dL_Al,1);
slope_Al = p_Al(1);
alpha_Al = slope_Al/50.8;
% invar data
temperature_I = [24 278]; % Celsius
displacement_I = [0 4.16]; % mm
displacement_I_inches = displacement_I * 0.0393701;
% relative change
dT_I = temperature_I - temperature_I(1);
```

```
dL_I = displacement_I_inches - displacement_I_inches(1);
p_I = polyfit(dT_I,dL_I,1);
slope_I = p_I(1);
alpha_I = slope_I/50.1;
% graph
figure;
plot(temperature_Al, dL_Al, 'o-');
hold on;
plot(temperature_I, dL_I, 's-');
title('Experimental Thermal Expansion Data: Aluminum vs Invar')
xlabel('Temperature (°C)');
ylabel('Displacement (inches)');
legend('Aluminum', 'Invar', 'Location', 'best');
grid on;
% compare
fprintf('Slope Aluminum: %.4e 1/°C\n', alpha_Al);
fprintf('Slope Invar: %.4e 1/°C\n', alpha_I);
fprintf('Al expands %.1f times more than Invar\n', alpha_Al/alpha_I);
```

Figure 8: MATLAB code for CTE test.

Figure 9: Jake Synder performing the vibrational test on the suspended prototype.

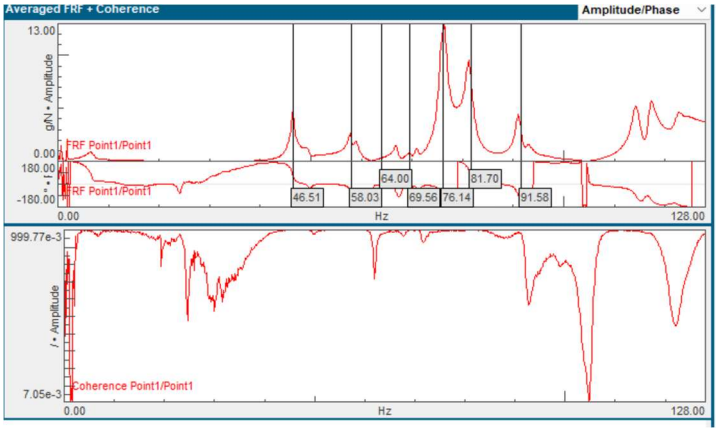

Figure 10: Experimental vibrational modes.

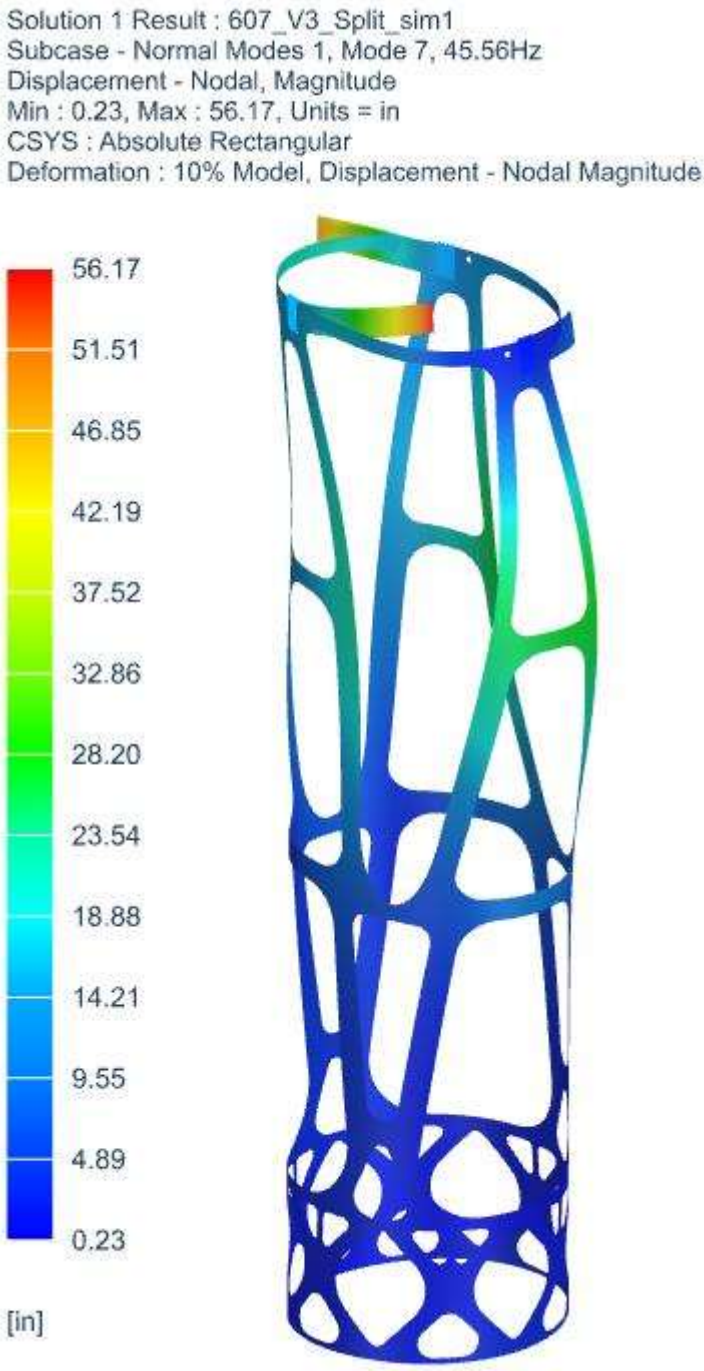

Figure 11: Free-free modal analysis to simulate vibrational test.

ANNEX E

MANUFACTURING

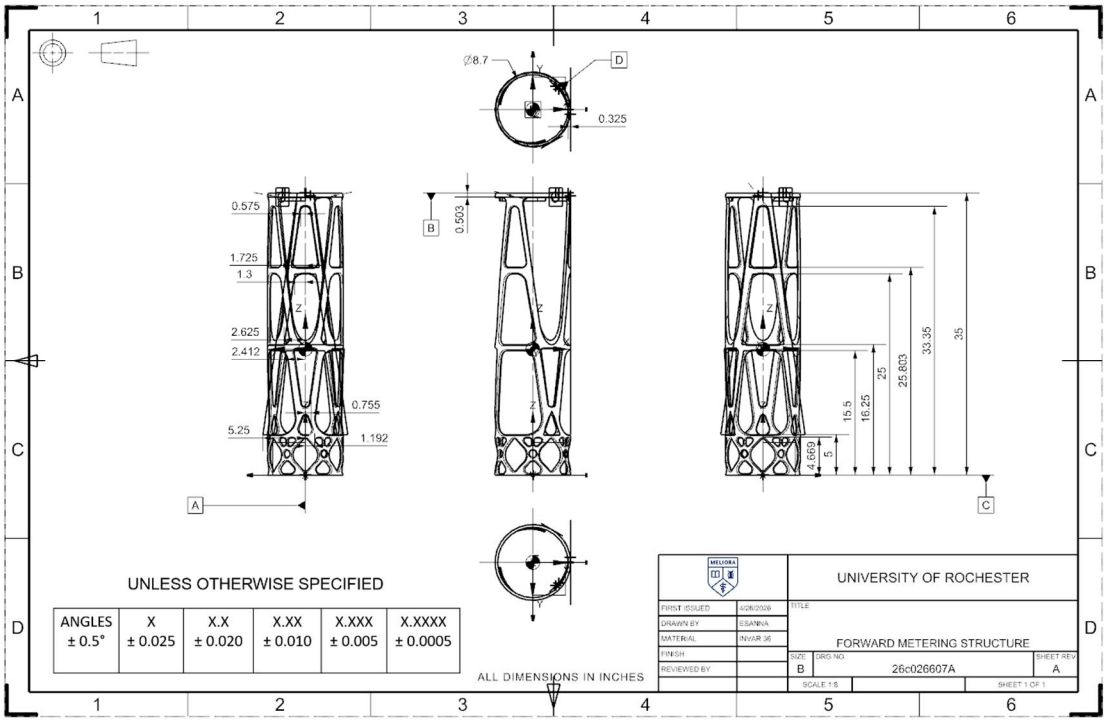

Figure 1: 2D CAD drawing of FMS.

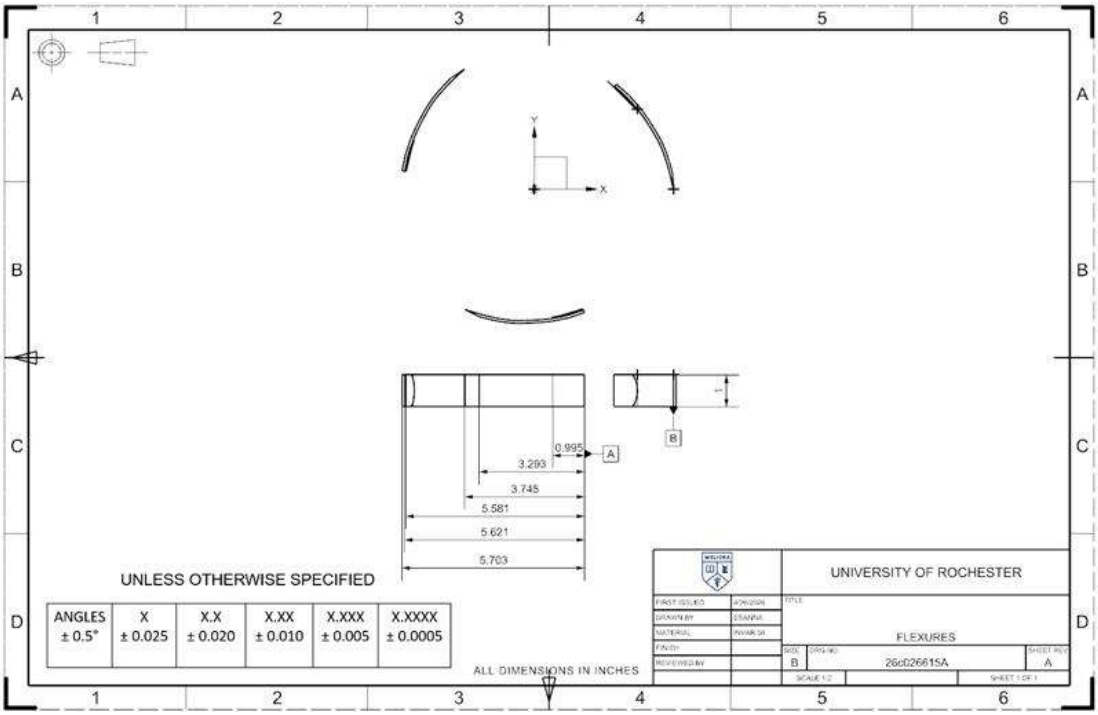

Figure 2: 2D CAD drawing of the Flexures.

Figure 3: 5/6 parts of the FMS assembled.

Figure 4: Zoom-in on printed supports.

Figure 5: Team members assembling the FMS.

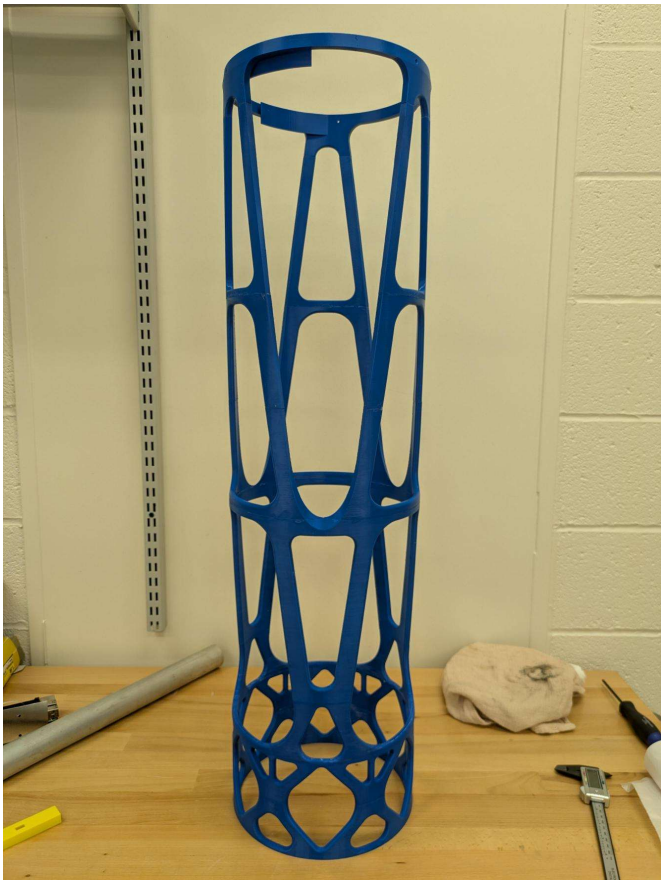

Figure 6: Fully assembled FMS.

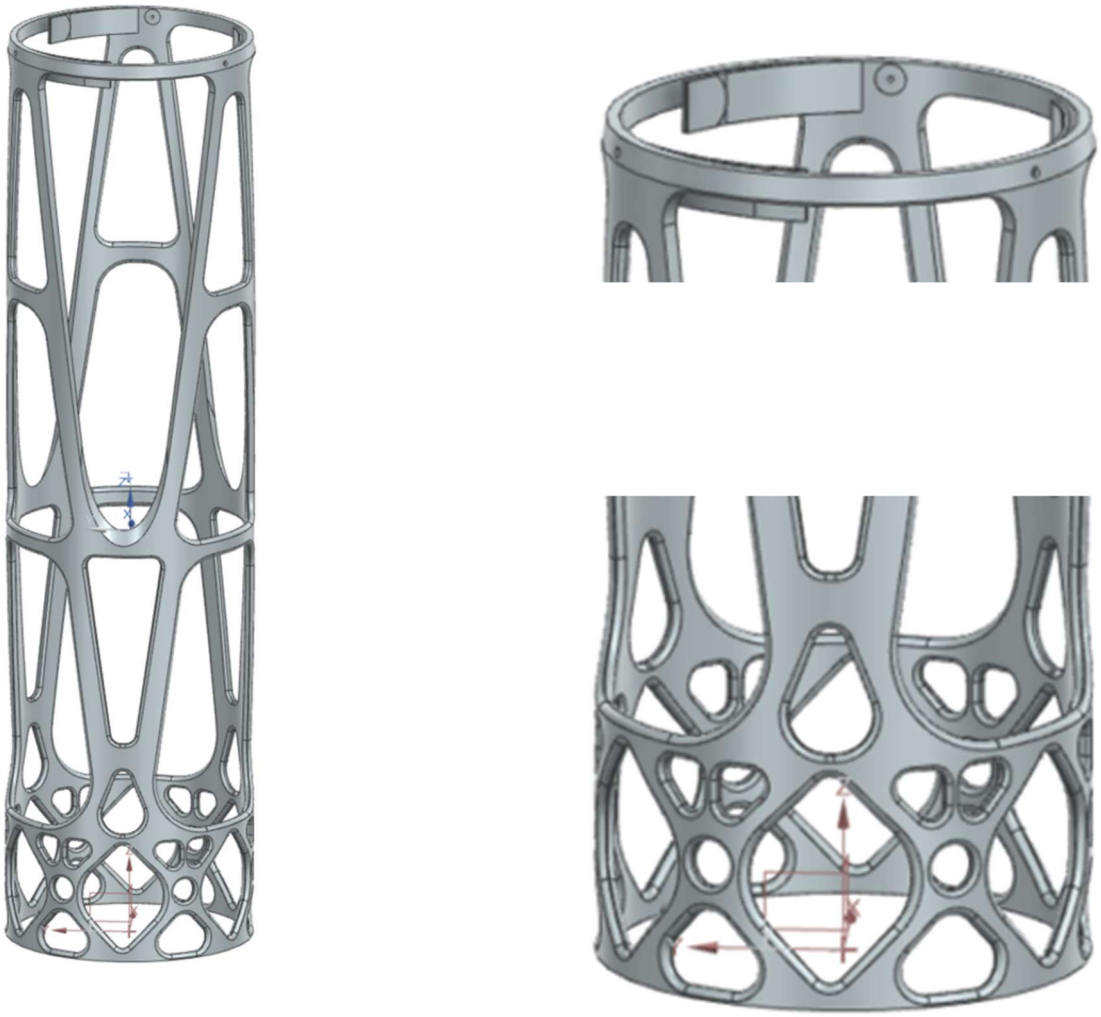

Figure 7: CAD model of final FMS design. RTV was changed to a circular geometry to decrease stress concentrations on the thin flexures. The base has also been optimized for weight, subtracting approximately 2.5 lbm whilst maintaining similar stiffness to previous designs.

ANNEX F

CALCULATIONS AND ANALYSIS

MODIFIED MATLAB INTERSECTION CODE

```
% U of R L3Harris Team, 3/21/2026, Modified from Devin Woodyard 2/12/2026, written with assistance from GPT
%
% This script reads a .model file from a 3MF file and plots it using the patch function.
%GPT Prompt: create a matlab script that take the .model text file from a 3MF file and plots it using the patch
function
%GPT Prompt: xmlreadstring is not a real command

clear
clc
%% INPUT 3MF File
% Define the 3MF file path and prompt user to use most recent or choose

% MARVIN NOTE - Change this to your file with the .3mf. It finds your most
% recent .3mf, but you can also manually pick it. This is where the .py
% will drop
%defaultFolder = fullfile('C:','Users','calde','Downloads','OneDrive_1_3-23-2026');
defaultFolder = fullfile('C:','X','ME205','FMS','3_23','OneDrive_1_3-23-2026');
if ~isfolder(defaultFolder)
    % Fallback to user's Downloads if the specified folder doesn't exist
    downloadsFolder = fullfile(getenv('USERPROFILE'), 'Downloads');
    if ~isfolder(downloadsFolder)
        downloadsFolder = fullfile(getenv('HOME'), 'Downloads'); % non-Windows fallback
    end
    defaultFolder = downloadsFolder;
end

% Look for .3mf files in the default folder
d = dir(fullfile(defaultFolder, '*.3mf'));
useFile = '';

if ~isempty(d)
    % Find most recently added .3mf by datenum (most recent file entry)
    % dir returns files sorted by name by default; use the datenum field to pick the most recently
added/modified
    [~, idx] = max([d.datenum]);
    mostRecentFile = fullfile(defaultFolder, d(idx).name);
    % Prompt the user
    choice = questdlg(sprintf('Use most recent .3mf in %s?\n\n%s', defaultFolder, d(idx).name), ...
        'Select 3MF File', ...
        'Recent','Select','Recent');
    switch choice
        case 'Recent'
            useFile = mostRecentFile;
        case 'Select'
            useFile = ''; % will trigger uigetfile below
        otherwise
            error('Operation cancelled by user.');
    end
end

% If no recent chosen or no files found, let user pick
if isempty(useFile)
    [fn, pn] = uigetfile({'*.3mf','3MF Files (*.3mf)'; '*.*','All Files (*.*)'}, 'Select 3MF file',
defaultFolder);
    if isequal(fn,0) || isequal(pn,0)
        error('No file selected. Operation cancelled.');
    end
    useFile = fullfile(pn, fn);
end

% Set filename and folder variables expected by the remainder of the script
[pn, fn_only, ext] = fileparts(useFile);
```

```
fn = [fn_only ext];
filename = fullfile(pn, fn);
outputname = 'urfms26_obex.mat';
%% Caclulations
% Unzip the 3MF file to extract the .model file
unzip(filename, 'temp_extracted');

% Define the path to the model file
modelFilePath = 'temp_extracted/3D/3dmodel.model';

% Read the content of the .model file
fileContent = fileread(modelFilePath);

% Write the content to a temporary XML file since xmlread reads from file
tempXmlFile = 'temp_model.xml';
fid = fopen(tempXmlFile, 'wt');
fprintf(fid, '%s', fileContent);
fclose(fid);

% Read the XML content
xmlData = xmlread(tempXmlFile);

% Extract vertex coordinates
geometryNodes = xmlData.getElementsByTagName('vertex');

% Extract face indices
triangleNodes = xmlData.getElementsByTagName('triangle');

% Parse the vertex and face data from the .model file
vertices = zeros(geometryNodes.getLength,3);
faces = zeros(triangleNodes.getLength,3);

% Extract vertex coordinates
for k = 0:geometryNodes.getLength-1
    vertex = geometryNodes.item(k);
    x = str2double(vertex.getAttribute('x'));
    y = str2double(vertex.getAttribute('y'));
    z = str2double(vertex.getAttribute('z'));
    vertices(k+1,:) = [x, y, z];
end

% Extract face indices
for k = 0:triangleNodes.getLength-1
    triangle = triangleNodes.item(k);
    v1 = str2double(triangle.getAttribute('v1')) + 1;
    v2 = str2double(triangle.getAttribute('v2')) + 1;
    v3 = str2double(triangle.getAttribute('v3')) + 1;
    faces(k+1,:) = [v1, v2, v3];
end


%% PLOT OUTPUT
% Plot the 3D model using the patch function
figure;
patch('Vertices', vertices, 'Faces', faces, 'FaceColor', 'c', 'EdgeColor', 'b');
axis equal;
grid on;
xlabel('X');
ylabel('Y');
zlabel('Z');
title('3MF Model Plot');
view(3);


%% FILE OUTPUT
save(outputname,"vertices","faces");


%% Clean Up
% Clean up
rmdir('temp_extracted', 's');
```

```
delete(tempXmlFile);


clear variables
close all

%% INPUTS
patchFile = 'urfms26_obex.mat';
linesFile = 'UR-FMS-020-RECT-2912.csv';
PM_ID = 10.35;


%% CALCULATIONS
% Load the patch data
load(patchFile, 'vertices', 'faces');

% Read the lines data from the .csv file
linesData = csvread(linesFile);

% Extract start and end coordinates
startPoints = linesData(:, 1:3);
endPoints = linesData(:, 4:6);

% Number of lines
numLines = size(startPoints, 1);

% Initialize intersection count
intersectCount = 0;

% Initialize obstruction data
obstructList = NaN(numLines,1);
nobstructList = obstructList;

% Create the figures
f1 = figure('Name','3D Obstruction','NumberTitle','Off');
hold on;

f2 = figure('Name','2D Obstruction','NumberTitle','Off');
hold on;

% Plot the patch
figure(f1);
patch('Vertices', vertices, 'Faces', faces, 'FaceColor', 'magenta', 'EdgeColor', 'black', 'FaceAlpha', 0.5);

% Check each line for intersection - optimized
% Precompute triangle data for Möller-Trumbore to avoid repeated work
numFaces = size(faces,1);
tri1 = vertices(faces(:,1), :);
tri2 = vertices(faces(:,2), :);
tri3 = vertices(faces(:,3), :);
edge1_all = tri2 - tri1;
edge2_all = tri3 - tri1;

% Parameters
epsilon = 1e-6;
PM_rad = PM_ID/2;

for i = 1:numLines
    % Get the start and end points of the line
    p1 = startPoints(i, :);
    p2 = endPoints(i, :);

    % Quick radial test: if start within PM area mark obstructed
    if (p1(1)^2 + p1(2)^2) < PM_rad^2
        intersectCount = intersectCount + 1;
        obstructList(i) = i;
        continue;
    end

    % Prepare ray direction once
    dir = p2 - p1;
```

```
    % Vectorized-ish Möller-Trumbore over all triangles:
    % Compute h = cross(dir, edge2_all) for all faces
    h = cross(repmat(dir, numFaces,1), edge2_all, 2);
    a = dot(edge1_all, h, 2);

    % Cull near-parallel triangles
    parallelMask = (a > -epsilon) & (a < epsilon);
    validMask = ~parallelMask;
    if ~any(validMask)
        % No valid triangles to test
        plot3([p1(1), p2(1)], [p1(2), p2(2)], [p1(3), p2(3)], 'b', 'LineWidth', 2);
        nobstructList(i) = i;
        continue;
    end

    f = zeros(numFaces,1);
    f(validMask) = 1 ./ a(validMask);

    s = repmat(p1, numFaces, 1) - tri1;
    u = f .* dot(s, h, 2);
    uMask = (u >= 0) & (u <= 1) & validMask;
    if ~any(uMask)
        plot3([p1(1), p2(1)], [p1(2), p2(2)], [p1(3), p2(3)], 'b', 'LineWidth', 2);
        nobstructList(i) = i;
        continue;
    end

    q = cross(s, edge1_all, 2);
    v = f .* dot(repmat(dir, numFaces,1), q, 2);
    uvMask = (v >= 0) & ((u + v) <= 1) & uMask;
    if ~any(uvMask)
        plot3([p1(1), p2(1)], [p1(2), p2(2)], [p1(3), p2(3)], 'b', 'LineWidth', 2);
        nobstructList(i) = i;
        continue;
    end

    t = f .* dot(edge2_all, q, 2);
    tMask = (t > epsilon) & uvMask;

    if any(tMask)
        % Intersection found
        intersectCount = intersectCount + 1;
        obstructList(i) = i;
        % Optionally plot intersecting ray (commented to speed up)
        % plot3([p1(1), p2(1)], [p1(2), p2(2)], [p1(3), p2(3)], 'r', 'LineWidth', 2);
    else
        % No intersection
        plot3([p1(1), p2(1)], [p1(2), p2(2)], [p1(3), p2(3)], 'b', 'LineWidth', 2);
        nobstructList(i) = i;
    end
end

%clean up obstruct and no obstruct lists
obstructList = rmmissing(obstructList);
nobstructList = rmmissing(nobstructList);

%create 2d plot
figure(f2)

% Line intersects, plot in 2d in red
figure(f2)
scatter(startPoints(obstructList,1),startPoints(obstructList,2),'r.');

% Line does not intersect, plot in 2d in blue
figure(f2)
scatter(startPoints(nobstructList,1),startPoints(nobstructList,2),'b.');

% Output the percentage of lines that intersect with the patch
percentIntersect = (intersectCount / numLines) * 100;
```

```
% Formatting the 3d plot
figure(f1)
title('PM to SM Ray Bundle Obstruction')
subtitle(sprintf('%.2f%% Obstruction\nPercent by Structure: %.2f', percentIntersect, percentIntersect - 10.85));
% xlabel('X (in)');
% ylabel('Y (in)');
% zlabel('Z (in)');
grid on;
axis equal;
hold off;
view([1 1 1])

% Formatting the plot
figure(f2)
title('Projected Obstruction')
subtitle(sprintf('%.2f%% Obstruction\nPercent by Structure: %.2f', percentIntersect, percentIntersect - 10.85));
% xlabel('X (in)');
% ylabel('Y (in)');
grid on;
axis equal;
hold off;

%% THIRD PLOT - Blocked Rays Only

f3 = figure('Name','Blocked Rays','NumberTitle','Off');
hold on

% Plot mesh obstruction
patch('Vertices', vertices, 'Faces', faces, ...
'FaceColor', 'magenta', ...
'EdgeColor', 'black', ...
'FaceAlpha', 0.3);

% Preallocate arrays for intersection points
interPts = zeros(length(obstructList), 3);
numInterPts = 0;

% Plot only obstructed rays (red, 50% opacity) and mark intersection points
for i = 1:length(obstructList)
    idx = obstructList(i);
    lineStart = startPoints(idx,:);
    lineEnd = endPoints(idx,:);

    % Plot the ray with 50% opacity
    plot3([lineStart(1) lineEnd(1)], ...
          [lineStart(2) lineEnd(2)], ...
          [lineStart(3) lineEnd(3)], ...
          'r','LineWidth',1.5,'Color',[1 0 0 0.5]); %#ok<NVREPL>

    % Find intersection point between this line and the mesh faces
    % Use the provided helper to check faces and compute intersection location
    dir = lineEnd - lineStart;
    numFaces = size(faces,1);
    tri1 = vertices(faces(:,1), :);
    tri2 = vertices(faces(:,2), :);
    tri3 = vertices(faces(:,3), :);
    edge1_all = tri2 - tri1;
    edge2_all = tri3 - tri1;

    % Vectorized Möller-Trumbore to get t values
    h = cross(repmat(dir, numFaces,1), edge2_all, 2);
    a = dot(edge1_all, h, 2);
    epsilon = 1e-6;
    valid = abs(a) > epsilon;
    if any(valid)
        f = zeros(numFaces,1); f(valid) = 1 ./ a(valid);
        s = repmat(lineStart, numFaces, 1) - tri1;
        u = f .* dot(s, h, 2);
        uMask = (u >= 0) & (u <= 1) & valid;
        if any(uMask)
            q = cross(s, edge1_all, 2);
```

```
            v = f .* dot(repmat(dir, numFaces,1), q, 2);
            uvMask = (v >= 0) & ((u + v) <= 1) & uMask;
            if any(uvMask)
                t = f .* dot(edge2_all, q, 2);
                tMask = (t > epsilon) & uvMask;
                if any(tMask)
                    % Take the smallest positive t (closest intersection)
                    [tval, tidx] = min(t(tMask));
                    % Map tidx back to global face index
                    maskIdx = find(tMask);
                    faceIdx = maskIdx(tidx);
                    intersectionPoint = lineStart + tval * dir;
                    numInterPts = numInterPts + 1;
                    interPts(numInterPts, :) = intersectionPoint;
                end
            end
        end
    end
end

% Trim unused preallocated rows
if numInterPts > 0
    interPts = interPts(1:numInterPts, :);
    % Plot intersection points as blue 'x' markers
    plot3(interPts(:,1), interPts(:,2), interPts(:,3), 'bx', 'MarkerSize', 8, 'LineWidth', 1.5);
end

title('Blocked Rays')
xlabel('X')
ylabel('Y')
zlabel('Z')
grid on
axis equal
view(3)
hold off


%% EXPORT INTERSECTED RAYS TO NX PYTHON SCRIPT (BLUE)

pyFile = 'plot_intersected_rays.py';
fid = fopen(pyFile, 'w');

fprintf(fid, 'import NXOpen\n\n');
fprintf(fid, 'def main():\n');
fprintf(fid, '    theSession = NXOpen.Session.GetSession()\n');
fprintf(fid, '    workPart = theSession.Parts.Work\n\n');

% Loop through intersected rays
for i = 1:length(obstructList)
    idx = obstructList(i);

    p1 = startPoints(idx,:);
    p2 = endPoints(idx,:);

    fprintf(fid, '    p1 = NXOpen.Point3d(%f, %f, %f)\n', p1(1), p1(2), p1(3));
    fprintf(fid, '    p2 = NXOpen.Point3d(%f, %f, %f)\n', p2(1), p2(2), p2(3));

    fprintf(fid, '    line = workPart.Curves.CreateLine(p1, p2)\n');

    %  BLUE + THICK
    fprintf(fid, '    disp = theSession.DisplayManager.NewDisplayModification()\n');
    fprintf(fid, '    disp.ApplyToAllFaces = False\n');
    fprintf(fid, '    disp.ApplyToOwningParts = False\n');
    fprintf(fid, '    disp.NewColor = 6\n'); % blue
    fprintf(fid, '    disp.NewWidth = NXOpen.DisplayableObject.ObjectWidth.Thick\n');
    fprintf(fid, '    disp.Apply([line])\n');
    fprintf(fid, '    disp.Dispose()\n\n');
end

fprintf(fid, 'if __name__ == "__main__":\n');
fprintf(fid, '    main()\n');
```

```
fclose(fid);

disp(['NX Python script created: ', pyFile]);

function intersect = checkLineFaceIntersections(vertices, faces, lineStart, lineEnd)
    intersect = false;
    for i = 1:size(faces, 1)
        faceVertices = vertices(faces(i, :), :);
        if lineIntersectsTriangle(lineStart, lineEnd, faceVertices)
            intersect = true;
            return;
        end
    end
end

function intersect = lineIntersectsTriangle(p1, p2, tri)
    % Use Möller-Trumbore intersection algorithm
    epsilon = 1e-6;
    edge1 = tri(2, :) - tri(1, :);
    edge2 = tri(3, :) - tri(1, :);
    h = cross(p2 - p1, edge2);
    a = dot(edge1, h);
    if a > -epsilon && a < epsilon
        intersect = false;
        return;
    end
    f = 1 / a;
    s = p1 - tri(1, :);
    u = f * dot(s, h);
    if u < 0.0 || u > 1.0
        intersect = false;
        return;
    end
    q = cross(s, edge1);
    v = f * dot(p2 - p1, q);
    if v < 0.0 || u + v > 1.0
        intersect = false;
        return;
    end
    t = f * dot(edge2, q);
    intersect = t > epsilon;
end
```

MATLAB CODE FOR PRELIMINARY DESIGN REVIEW CALCULATIONS

```
%% Tube Envelope Scaling Study (Shigley-style)
% Visualize stiffness, mass/weight, and "efficiency" trends vs wall thickness,
% and quantify change per 0.01" thickness step.

clear; clc; close all;

%% Tube Envelope Scaling Study (Shigley-style)
% Visualize stiffness, mass/weight, and "efficiency" trends vs wall thickness,
% and quantify change per 0.01" thickness step.
%
% Envelope constraint: max thickness is 0.625 in (Do=9.35, Di=8.10).
% Plots show x-axis from 0 to 0.625 for visualization, but calculations
% start at a small nonzero thickness to avoid A=0 and I/A undefined.
%
% NOTE: plots INCLUDE the origin on the x-axis, but
% the script does NOT add an artificial (0,0) data point.

clear; clc; close all;

%% ====== GIVEN ======
Do  = 9.35;                 % outer diameter [in] (fixed envelope)
L   = 33;                   % length [in]
```

```
rho = 0.293;                % lb/in^3 (often used as weight density in English units)
E   = 2.045e7;              % Young's modulus [psi]
nu  = 0.29;                 % Poisson's ratio [-]
G   = E/(2*(1+nu));         % shear modulus [psi]

%% ====== THICKNESS RANGE (ENVELOPE-LIMITED) ======
% Do NOT compute at t=0 (A=0 causes I/A undefined, percent changes blow up).
t_min = 0.01;               % [in] small but nonzero
t_max = 0.625;              % [in] envelope max thickness
dt    = 0.001;              % [in] resolution for smooth curves
t = (t_min:dt:t_max)';      % column vector thicknesses

%% ====== GEOMETRY ======
Di = Do - 2*t;              % inner diameter [in]
ro = Do/2;                  % [in]
ri = Di/2;                  % [in]

% Section properties (hollow circular tube)
A = pi*(ro^2 - ri.^2);                  % area [in^2]
I = (pi/4)*(ro^4 - ri.^4);              % area MOI [in^4]
J = (pi/2)*(ro^4 - ri.^4);              % polar MOI [in^4] (=2I)

%% ====== MASS / WEIGHT ======
V   = A*L;                  % volume [in^3]
W   = rho*V;                % "weight" [lb] if rho treated as weight density
WpL = rho*A;                % weight per length [lb/in]

%% ====== STIFFNESS (Shigley Ch. 4) ======
% Axial stiffness: k_ax = AE/L
Kax = (A*E)/L;                          % [lbf/in]

% Cantilever tip lateral stiffness: k_bend = 3EI/L^3
Kbend = (3*E*I)/(L^3);                  % [lbf/in]

% Torsional stiffness: k_tor = GJ/L
Ktor = (G*J)/L;                         % [lbf*in/rad]

%% ====== "EFFICIENCY" METRICS (stiffness per weight proxy) ======
% For fixed L and rho, stiffness-per-weight proxies reduce to I/A and J/A.
Eff_bend = I./A;         % bending efficiency proxy [in^2]
Eff_tor  = J./A;         % torsion efficiency proxy [in^2]

%% ====== CHANGE PER 0.01" THICKNESS STEP ======
step = 0.01;

% Forward-step deltas: Y(t+0.01) - Y(t)
t2 = t + step;
valid = t2 <= t_max;

% Interpolate properties at t+0.01 then subtract
A2     = interp1(t, A,        t2(valid), "linear");
I2     = interp1(t, I,        t2(valid), "linear");
J2     = interp1(t, J,        t2(valid), "linear");
W2     = interp1(t, W,        t2(valid), "linear");
Kax2   = interp1(t, Kax,      t2(valid), "linear");
Kbend2 = interp1(t, Kbend,    t2(valid), "linear");
Ktor2  = interp1(t, Ktor,     t2(valid), "linear");
Eb2    = interp1(t, Eff_bend, t2(valid), "linear");
Et2    = interp1(t, Eff_tor,  t2(valid), "linear");

dA_001     = A2     - A(valid);
dI_001     = I2     - I(valid);
dJ_001     = J2     - J(valid);
dW_001     = W2     - W(valid);
dKax_001   = Kax2   - Kax(valid);
dKbend_001 = Kbend2 - Kbend(valid);
dKtor_001  = Ktor2  - Ktor(valid);
dEffB_001  = Eb2    - Eff_bend(valid);
dEffT_001  = Et2    - Eff_tor(valid);

% Percent changes per +0.01"
```

```
pct = @(dY,Y) 100*(dY./Y);
pW_001     = pct(dW_001,     W(valid));
pKax_001   = pct(dKax_001,   Kax(valid));
pKbend_001 = pct(dKbend_001, Kbend(valid));
pKtor_001  = pct(dKtor_001,  Ktor(valid));
pEffB_001  = pct(dEffB_001,  Eff_bend(valid));
pEffT_001  = pct(dEffT_001,  Eff_tor(valid));

%% ====== PLOT 1: Weight and stiffness vs thickness ======
figure;
plot(t, W, t, Kax, t, Kbend, t, Ktor, "LineWidth", 1.5);
grid on; xlabel("Wall thickness t [in]");
ylabel("Value (mixed units)");
title("Weight and Stiffness vs Wall Thickness (OD fixed)");
legend("W [lb]", "Kax [lbf/in]", "Kbend [lbf/in]", "Ktor [lbf*in/rad]", "Location","best");
xlim([0 0.625]);  % includes origin on axis, no artificial (0,0) point added

%% ====== PLOT 2: Efficiency vs thickness ======
figure;
plot(t, Eff_bend, t, Eff_tor, "LineWidth", 1.5);
grid on; xlabel("Wall thickness t [in]");
ylabel("Efficiency proxy [in^2] (I/A or J/A)");
title("Stiffness-per-Weight Proxies vs Wall Thickness");
legend("I/A (bending efficiency)", "J/A (torsion efficiency)", "Location","best");
xlim([0 0.625]);

%% ====== PLOT 3: Stiffness vs weight trade ======
figure;
plot(W, Kbend, W, Ktor, W, Kax, "LineWidth", 1.5);
grid on; xlabel("W [lb]");
ylabel("Stiffness (mixed units)");
title("Stiffness vs Weight Trade (OD fixed, varying thickness)");
legend("Kbend [lbf/in]", "Ktor [lbf*in/rad]", "Kax [lbf/in]", "Location","best");

%% ====== PLOT 4: Absolute change per +0.01" thickness step ======
figure;
subplot(3,1,1);
plot(t(valid), dW_001, "LineWidth", 1.5); grid on;
ylabel("\Delta W per +0.01 [lb]");
title("Absolute Change per +0.01 in Thickness");
xlim([0 0.625]);

subplot(3,1,2);
plot(t(valid), dKbend_001, t(valid), dKtor_001, t(valid), dKax_001, "LineWidth", 1.5); grid on;
ylabel("\Delta K per +0.01");
legend("\Delta Kbend", "\Delta Ktor", "\Delta Kax", "Location","best");
xlim([0 0.625]);

subplot(3,1,3);
plot(t(valid), dEffB_001, t(valid), dEffT_001, "LineWidth", 1.5); grid on;
xlabel("Wall thickness t [in]");
ylabel("\Delta (I/A), \Delta (J/A)");
legend("\Delta(I/A)", "\Delta(J/A)", "Location","best");
xlim([0 0.625]);

%% ====== PLOT 5: Percent change per +0.01" thickness step ======
figure;
subplot(3,1,1);
plot(t(valid), pW_001, "LineWidth", 1.5); grid on;
ylabel("%\Delta W per +0.01");
title("Percent Change per +0.01 in Thickness");
xlim([0 0.625]);

subplot(3,1,2);
plot(t(valid), pKbend_001, t(valid), pKtor_001, t(valid), pKax_001, "LineWidth", 1.5); grid on;
ylabel("%\Delta K per +0.01");
legend("%\Delta Kbend", "%\Delta Ktor", "%\Delta Kax", "Location","best");
xlim([0 0.625]);

subplot(3,1,3);
plot(t(valid), pEffB_001, t(valid), pEffT_001, "LineWidth", 1.5); grid on;
```

```
xlabel("Wall thickness t [in]");
ylabel("%\Delta efficiency per +0.01");
legend("%\Delta(I/A)", "%\Delta(J/A)", "Location","best");
xlim([0 0.625]);

%% ====== OPTIONAL: Mark the three design points ======
t_pts = [0.625; 0.25; 0.10];
t_pts = t_pts(t_pts>=t_min & t_pts<=t_max);

W_pts     = interp1(t, W,     t_pts);
Kbend_pts = interp1(t, Kbend, t_pts);

fig = figure;
ax = axes(fig);

% --- Force backgrounds (plot area white, surrounding area light gray) ---
set(fig,'Color',[0.93 0.93 0.93]);   % figure background (outside axes): light gray
set(ax,'Color','w');                 % axes background (plot area): white

% Ensure axes/text are visible and not stuck in dark-theme colors
set(ax,'XColor','k','YColor','k');
set(ax,'GridColor',[0.75 0.75 0.75]);

% Plot main curve (hot pink)
hp = plot(ax, W, Kbend, '-', ...
    'LineWidth', 2.5, ...
    'Color', [1 0 0.6]);   % hot pink-ish (RGB)

hold(ax,'on');

% Plot case points (solid black dots)
plot(ax, W_pts, Kbend_pts, 'o', ...
    'MarkerSize', 9, ...
    'MarkerFaceColor', 'k', ...
    'MarkerEdgeColor', 'k', ...
    'LineWidth', 1.5);

% Labels/title
grid(ax,'on');
xlabel(ax,'W [lb]');
ylabel(ax,'K_{bend} [lbf/in]');
title(ax,'K_{bend} vs Weight');

% Make all text/axes black (important if a dark theme is active)
set(ax, 'XColor','k', 'YColor','k');     % tick marks + axes lines
set(ax, 'GridColor',[0.75 0.75 0.75]);   % light gray grid
set(ax, 'MinorGridColor',[0.85 0.85 0.85]);

% Optional: turn off scientific notation if you want
% ax.YAxis.Exponent = 0;

% Legend (optional)
legend(ax, {'Curve','Cases'}, 'Location','southeast');

% Make exported image keep colors
set(fig,'InvertHardcopy','off');
exportgraphics(fig,'Kbend_vs_Weight_clean.png','Resolution',300);

%% ====== QUICK CONSOLE OUTPUT AT THE THREE CASES ======
A_pts    = interp1(t, A,    t_pts);
I_pts    = interp1(t, I,    t_pts);
J_pts    = interp1(t, J,    t_pts);
Kax_pts  = interp1(t, Kax,  t_pts);
Ktor_pts = interp1(t, Ktor, t_pts);

fprintf("\n--- Values at the three thickness cases ---\n");
for i = 1:numel(t_pts)
    fprintf("t = %.3f in: A=%.3f, I=%.3f, J=%.3f, W=%.2f, Kax=%.3e, Kbend=%.3e, Ktor=%.3e\n", ...
        t_pts(i), A_pts(i), I_pts(i), J_pts(i), W_pts(i), Kax_pts(i), Kbend_pts(i), Ktor_pts(i));
end
```

MATLAB CODE FOR EARLY FLEXURE REVIEW

```
%% Simple Shear MOS Screening for Multiple Flexure Designs
% This script uses ONLY the first/simple hand calc:
%   A = D*t
%   total shear area = num_blades * A
%   stress = force / total shear area
%   MOS = YS_shear / (stress * FOS) - 1
%
% It compares multiple design concepts by changing only the number of
% load-sharing blades.
%
% IMPORTANT:
% This script does NOT account for flexure length.
% It is only a first-pass shear/MOS sizing screen based on equations provided by L3Harris

clear; clc; close all;

%% ---------------- USER INPUTS ----------------
D = 1;                      % Blade depth [in]
mass_SM = 4.1;              % Mirror mass-like input
g_load = 30;                % 30g load factor
g_conv = 32.174;            % Conversion factor used in original script

YS_tensile = 34800;         % psi
FOS = 2;                    % yield FOS
YS_shear = 0.577 * YS_tensile;

t_print_min = 0.016;        % in
t_max = 0.25;               % in
dt = 1e-4;                  % in

%% ---------------- TOTAL FORCE ----------------
force_shear = g_load * mass_SM * g_conv;   % lbf (based on current setup)

%% ---------------- DESIGN DEFINITIONS ----------------
designs = struct([]);

% 1) One-way straight: 3 total blades
designs(1).name = 'OneWayStraight';
designs(1).num_blades = 3;

% 2) Two-way straight: 6 total blades
designs(2).name = 'TwoWayStraight';
designs(2).num_blades = 6;

% 3) Curved one-way: 3 total blades
designs(3).name = 'CurvedOneWay';
designs(3).num_blades = 3;

% 4) Curved two-way: 6 total blades
designs(4).name = 'CurvedTwoWay';
designs(4).num_blades = 6;

%% ---------------- THICKNESS SWEEP ----------------
t_vals = t_print_min:dt:t_max;

results = struct([]);

for d = 1:numel(designs)

    num_blades = designs(d).num_blades;

    % Closed-form solution for MOS = 0
    t_required_closed = (force_shear * FOS) / (num_blades * D * YS_shear);

    % Sweep calculation
    A_blade = D .* t_vals;                % area per blade [in^2]
    A_total = num_blades .* A_blade;      % total shear area [in^2]
    stress_vals = force_shear ./ A_total;  % shear stress [psi]
```

```
    MOS_vals = YS_shear ./ (stress_vals .* FOS) - 1;

    idx = find(MOS_vals > 0, 1, 'first');

    if isempty(idx)
        t_required_sweep = NaN;
    else
        t_required_sweep = t_vals(idx);
    end

    % Store results
    results(d).name = designs(d).name;
    results(d).num_blades = num_blades;
    results(d).t_required_closed = t_required_closed;
    results(d).t_required_sweep = t_required_sweep;
    results(d).MOS_vals = MOS_vals;
end

%% ---------------- PRINT RESULTS ----------------
fprintf('\n=====================================================\n');
fprintf('SIMPLE SHEAR MOS SCREENING RESULTS\n');
fprintf('=====================================================\n');

for d = 1:numel(results)
    fprintf('\nDesign: %s\n', results(d).name);
    fprintf('  Total load-sharing blades = %d\n', results(d).num_blades);
    fprintf('  Closed-form t for MOS = 0: %.6f in\n', results(d).t_required_closed);

    if isnan(results(d).t_required_sweep)
        fprintf('  No positive MOS found in sweep range.\n');
    else
        fprintf('  Sweep minimum passing thickness: %.6f in\n', results(d).t_required_sweep);
    end
end

%% ---------------- PLOT ----------------
figure('Color','w');
hold on; grid on; box on;

for d = 1:numel(results)
    plot(t_vals, results(d).MOS_vals, 'DisplayName', results(d).name);
end

yline(0, '--k', 'MOS = 0');
xlabel('Blade Thickness, t [in]');
ylabel('Margin of Safety (MOS)');
title('Simple Shear MOS vs Thickness for Each Design');
legend('Location','best');
```